Isogeometric Analysis of the Navier–Stokes–Cahn–Hilliard equations with application to incompressible two-phase flows

Babak S. Hosseini[a,*], Stefan Turek[a], Matthias Möller[b], Christian Palmes[a]

[a] *TU Dortmund, Institute of Applied Mathematics (LS III), Vogelpothsweg 87, 44227 Dortmund, Germany*
[b] *Delft University of Technology, Delft Institute of Applied Mathematics, Mekelweg 4, 2628 CD Delft, The Netherlands*

Abstract

In this work, we provide a unified and comparative description of the most prominent phase field based two-phase flow models and present our numerical results of the application of Galerkin-based Isogeometric Analysis (IGA) to incompressible Navier–Stokes–Cahn–Hilliard (NSCH) equations in velocity–pressure–phase field–chemical potential formulation. For the approximation of the velocity and pressure fields, LBB compatible non-uniform rational B-spline spaces are used which can be regarded as smooth generalizations of Taylor–Hood pairs of finite element spaces. The one-step θ-scheme is used for the discretization in time. The static and rising bubble, in addition to the nonlinear Rayleigh-Taylor instability flow problems, are considered in two dimensions as model problems in order to investigate the numerical properties of the scheme.

Keywords: Two-phase flow, Cahn–Hilliard phase field model, Navier–Stokes–Cahn–Hilliard equations, Isogeometric Analysis, Isogeometric finite elements, B-splines/NURBS, Rising bubble, Rayleigh–Taylor instability

1. Introduction

Multiphase flows of immiscible fluids, that is, flow of fluids which are incapable of mixing, such as e.g. oil and water, are omnipresent in nature and industrial systems. By way of example we refer to the Deepwater Horizon oil spill in the gulf of Mexico and the respective industrial plant in charge with pumping an oil water mixture to the surface. In particular, in a multiphase flow context the dynamics of bubbles and droplets including their deformation, coalescence and breakup are intriguing processes which have gained a lot of attention in the scientific community, cf. [4, 6, 22, 25, 26]. In two-phase flows, being the most common multiphase flow configuration involving two distinct fluids, the fluids are segregated by a very thin interfacial region where surface tension effects and mass transfer due to chemical reactions may appear. The former is caused by molecular force imbalances in the vicinity of the fluid interface. The extension of the physical model to multiple fluids, with each fluid being allowed to have its own density and viscosity, comes at a cost of potentially sharp gradients of these quantities and pressure jumps across the phase separating interface. As for methodologies to address these issues, the sharp- and diffuse-interface methods are among the most widely used ones to model fluid interface dynamics. Traditionally, phase transition phenomena have been described with sharp interface models. This involves the tracking of the phase separating interface as it evolves over time. Among Eulerian interface tracking methods the volume-of-fluid

*Corresponding author
Email addresses: babak.hosseini@math.tu-dortmund.de (Babak S. Hosseini), stefan.turek@math.tu-dortmund.de (Stefan Turek), m.moller@tudelft.nl (Matthias Möller), christian.palmes@tu-dortmund.de (Christian Palmes)

[19] and the level-set [31] method constitute the most prominent sharp interface models and have been applied in a multitude of multiphase applications. However, especially in the realization of the latter method discontinuous functions are often regularized and artificially "smoothed" with regularized Heaviside or step functions. The regularization aids to circumvent problems with numerical integration when discontinuous coefficients and functions are involved. Henceforth, the level-set method can sometimes be regarded as a diffuse interface method as well, since it introduces a narrow transition region across which the regularization of discontinuous coefficients is realized.

In this work we use a phase field diffuse interface method based on the Cahn–Hilliard (CH) equation and apply Isogeometric Analysis for the discretization of the involved equations. Diffuse-interface models have been used in a wide spectrum of fields, ranging from material sciences to fracture mechanics. Moreover, in recent years they have been successfully used to describe the flow of two or more immiscible fluids for both numerical and theoretical studies. Particularly for two-phase flows, they have gained a lot of attention due to their ability to easily handle moving contact lines and topological transitions without any need for reinitialization or advective stabilization. On a general note, diffuse interface models allow the modeling of interfacial forces as continuum forces with the effect that delta-function forces and discontinuities at the interface are smoothed by smearing them over thin yet numerically resolvable layers. The phase field method - also known as the diffuse interface model - is based on models of fluid free energy and offers a systematic physical approach by describing the interface in a physical rather than in a numerical sense. One principal advantage of diffuse interface models is their ability to describe topological transitions like droplet coalescence or break-up in a natural way. In the phase field framework, the interface is modeled by a function $\varphi(x,t)$ which represents the concentration of the fluids. The function $\varphi(x,t)$, also referred to as the order parameter, or the phase field, attains a distinct constant value in each phase and rapidly, but smoothly, changes in the interface region between the phases. For a binary fluid, a usual assumption is that φ takes values between -1 and 1, or 0 and 1. The relaxation of the order parameter is driven by local minimization of the fluid free energy subject to the phase field conservation. As a result, complex interface dynamics such as coalescence or segregation can be captured without any special procedures [3, 35].

The mathematical modeling of phase field-based two-phase incompressible flows dates at least back to the work of Gurtin et al. [17] and has originated a multitude of different models ever since. These models differ from each other by a group of quite diverse criteria, one of them being e.g. the treatment of the density, that is, considering it constant or variable. Moreover, not all models are based on a divergence-free velocity field and the modeling of extra contributions of additional forces to the stress tensor such as e.g. the surface tension induced capillary forces is quite varied across the models. While for some models no energy inequalities are known, others are shown to admit an energy law and to be thermodynamically consistent. For the latter to hold, some of the affected models are extended by additional terms. Each of these models has its own advantages and disadvantages in terms of suitability for particular flow scenarios, physical consistency and implementation simplicity. Following the agenda to assess Isogeometric Analysis-based approximations of various variable density two-phase flow problems with respect to reference "sharp interface"-based results, the identification of a reasonable model turned up to be a time consuming and tedious process. This is founded on the fact that there are quite a number of different models at one's disposal, each having a distinct set of traits determining its overall suitability. As an additional reason, we identify the lack of a consolidated inventory with emphasis on the most essential features and shortcomings of each model. In order to address this issue and to make this article self contained, we have decided to briefly present and screen the models in a dedicated section (see Section 2).

Using the numerical benchmark setups of Hysing et al. [22] for two-dimensional bubble dynamics,

Aland et al. [2] compared three different phase field-based incompressible two-phase flow models utilizing a classical finite element discretization. More specifically, the results computed with the models of Ding, Boyer and Abels (see Section 2) are compared to both each other and to those of Hysing being based on a level-set sharp interface model. The performed numerical analysis indicates a good result-wise agreement among all three phase field models and in particular exhibits rather small differences between the models of Ding and Abels. Using this finding, we identify the model proposed by Ding as suitable for our purposes and apply Isogeometric Analysis to the above mentioned two-phase flow benchmark problems. To our best knowledge this is the first work aiming to recover Hysing's sharp interface based variable density and variable viscosity two-phase flow benchmark results applying Isogeometric Analysis to a NSCH model. Besides, the robustness of the Isogeometric discretization of the NSCH system is further underpinned by its application to other challenging two-phase flow scenarios such as for instance the "Rayleigh–Taylor instability".

We consider the combination of Isogeometric Analysis and the NSCH system for the numerical treatment of multiphase flow problems as very powerful. This is attributed on the one hand to the above mentioned benefits of phase field methods, and on the other hand to the ability to perform finite element type numerical analysis on complex geometries without the necessity to discretize it with straight line segments or flat faces. This has proven in a row of different context to yield gains in accuracy compared to alternative numerical methods [8]. Moreover, the Cahn-Hilliard equation in its primal formulation involves fourth order spatial derivatives requiring $\mathcal{C}^1$ continuous discrete approximation spaces which can easily be spanned with high regularity basis functions in Isogeometric Analysis.

As of writing of this article there are in all conscience two other works combining Isogeometric Analysis with the advective Cahn–Hilliard phase field model and fluid flow. The first article [29] uses the advective Cahn–Hilliard equation and presents an Isogeometric Analysis-based numerical study of spinodal decomposition of a binary fluid undergoing shear flow. In contrast to this work, however, they use a passive and externally provided velocity field and in particular do not solve a coupled NSCH system. The second work [12] on the other hand, aims to analyze the dynamics of liquid droplets in a liquid continuum. It does involve a NSCH system and utilizes divergence-free B-spline spaces to obtain a discrete pointwise divergence-free velocity field. The focus of that work is on the energy exchange analysis in droplet dynamics, or more specifically, on the analysis of the exchanges of the kinetic, potential, bulk and interfacial free energies as droplets start to merge. However, in contrast to this article, they use an NSCH model under the Boussinesq assumption to account for buoyancy effects. This imposes a severe constraint on the admitted density differences, in fact in their work they assume small density differences between the fluids while we go up to density ratio 1000.

The outline of this article is as follows: In Section 2 we follow the agenda to identify and select an adequate phase field-based two-phase flow model and provide therefore a concise traits-oriented characterization and comparison of the most significant models. The mathematical model used in this work is eventually described in Section 3 serving as a basis for Section 4 that is in turn dedicated to the discretization aspects of the mathematical model with Isogeometric Analysis. We present our numerical results in Section 5 and conclude the article with a short summary in Section 6.

2. Phase field-based two-phase flow models

When it comes to the coupling of phase segregation with hydrodynamics, the basic diffuse interface model for two incompressible, viscous Newtonian fluids is the so called "Model H" [17, 20] which was derived in the framework of rational continuum mechanics and is shown to satisfy the second law of thermodynamics in a mechanical version based on local dissipation inequality. It leads

to the coupled Navier–Stokes–Cahn–Hilliard (NSCH) system

$$\rho\partial_t \boldsymbol{v} + \rho\left(\boldsymbol{v}\cdot\nabla\right)\boldsymbol{v} - \operatorname{div}\left(2\mu(\varphi)\frac{1}{2}\left(\nabla\boldsymbol{v} + (\nabla\boldsymbol{v})^T\right)\right) + \nabla p = -\hat{\sigma}\varepsilon\operatorname{div}\left(\nabla\varphi\otimes\nabla\varphi\right), \tag{1.1}$$

$$\operatorname{div}\boldsymbol{v} = 0, \tag{1.2}$$

$$\partial_t\varphi + \boldsymbol{v}\cdot\nabla\varphi = \operatorname{div}\left(m\nabla\eta\right), \tag{1.3}$$

$$\eta = \hat{\sigma}\varepsilon^{-1}\psi'(\varphi) - \hat{\sigma}\varepsilon\Delta\varphi, \tag{1.4}$$

where $\rho, \mu(\varphi), \boldsymbol{v}$ and p denote the density, dynamic viscosity, mean velocity, and pressure, respectively and φ is the order parameter related to the concentration of the fluids (e.g. concentration of one component). Moreover, $\hat{\sigma}$ is the surface energy density coefficient, ε is a parameter related to the thickness of the interfacial region, ψ denotes the homogeneous free energy density function, $m = m(\varphi)$ is the mobility coefficient and μ is the chemical potential. The term $\hat{\sigma}\varepsilon\left(\nabla\varphi\otimes\nabla\varphi\right)$ on the right hand side of (1.1) represents surface tension induced capillary forces and is modeled as an extra contribution in the stress tensor. The modeling assumption of constant density ρ in both components as well as in the transition region, unfortunately entails a severe constraint on the usability of this model and restricts its applicability to situations with negligible density differences. In order to nevertheless account for buoyancy effects in the treatment of problems with small density ratios, a customary practice is to use a Boussinesq approximation, that is, considering the density constant except when multiplying it with the gravitational force field $\boldsymbol{g}$.

In order to overcome the constant density constraint, the following thermodynamically consistent extension of Model H for different densities was derived by Lowengrub and Truskinovsky [30]

$$\rho\partial_t \boldsymbol{v} + \rho\left(\boldsymbol{v}\cdot\nabla\right)\boldsymbol{v} - \operatorname{div}\boldsymbol{S}\left(\varphi, \boldsymbol{D}(\boldsymbol{v})\right) + \nabla p = -\hat{\sigma}\varepsilon\operatorname{div}\left(\nabla\varphi\otimes\nabla\varphi\right), \tag{2.1}$$

$$\partial_t\rho + \operatorname{div}(\rho\boldsymbol{v}) = 0, \tag{2.2}$$

$$\rho\partial_t\varphi + \rho\boldsymbol{v}\cdot\nabla\varphi = \operatorname{div}\left(m(\varphi)\nabla\eta\right), \tag{2.3}$$

$$\eta = -\rho^{-2}\frac{\partial\rho}{\partial\varphi}p + \frac{\hat{\sigma}}{\varepsilon}\psi'(\varphi) - \frac{\hat{\sigma}\varepsilon}{\rho}\operatorname{div}\left(\rho\nabla\varphi\right), \tag{2.4}$$

where $\boldsymbol{D}(\boldsymbol{v}) = \frac{1}{2}\left(\nabla\boldsymbol{v} + (\nabla\boldsymbol{v})^T\right), \boldsymbol{S}\left(\varphi, \boldsymbol{D}(\boldsymbol{v})\right) = 2\mu(\varphi)\boldsymbol{D}(\boldsymbol{v}) + \lambda(\varphi)\operatorname{div}\boldsymbol{v}\,\boldsymbol{I}$ and $\lambda(\varphi)$ is the bulk viscosity coefficient. Equation (2) defines the mean velocity $\boldsymbol{v}$ as a mass averaged or barycentric velocity $\rho\boldsymbol{v} = \rho_1\boldsymbol{v}_1 + \rho_2\boldsymbol{v}_2$, where ρ_j and $\boldsymbol{v}_j$ with $j = 1, 2$ denote the densities and velocities of the individual fluids. It is necessary to point out though that this velocity is not divergence-free. In the above system the coupling of the Navier-Stokes (2.1)-(2.2) and the Cahn–Hilliard terms (2.3)-(2.4) is much stronger that in the classical Model H, since the fluid pressure p enters the equation of the chemical potential η and thus aggravates numerical simulations. An additional difficulty is introduced by the non-solenoidal velocity field for which no solution concept is available which avoids to determine the pressure p.

Despite the fact that simplifications of this model have successfully been used in numerical studies [27, 28], to the best of the author's knowledge, until recently there were no discrete schemes available being based on the full model (2.1)-(2.4). In recent years, however, different numerical schemes have been developed by the groups of Lowengrub and Giesselmann, cf. [16, 23].

Ding [10] and Boyer [5] each came up with alternative generalizations of Model H for different densities. Their starting point are the equations for the mass conservation of each phase

$$\frac{\partial\rho_j}{\partial t} + \operatorname{div}(\rho_j\boldsymbol{v}_j) = 0 \tag{3}$$

eventually yielding a divergence-free $\nabla\cdot\boldsymbol{v} = 0$ velocity field. Moreover, their definition of the mean velocity $\boldsymbol{v}$ of the mixture differs from that of Lowengrub and Truskinovsky inasmuch as it is defined

to be the volume averaged velocity $\boldsymbol{v} = u_1\boldsymbol{v}_1 + u_2\boldsymbol{v}_2$ with u_j denoting the volume fraction of fluid j. The model proposed by Ding is basically a generalization of (1) for variable densities $\rho(\varphi)$, while the more complicated model presented by Boyer

$$\rho(\varphi) = 1 + \frac{\varepsilon}{2}(\varphi - 1), \tag{4.1}$$

$$\rho(\varphi)\left(\frac{\partial \boldsymbol{v}}{\partial t} + \boldsymbol{v}\cdot\nabla\boldsymbol{v}\right) - \frac{1}{Re}\mathrm{div}\left(2\mu(\varphi)\boldsymbol{D}(\boldsymbol{v})\right) + \nabla p = \mathcal{K}\eta\nabla\varphi + \varepsilon\mathcal{K}\frac{1-\varphi^2}{4}\nabla\left(\frac{\eta}{\rho(\varphi)}\right) + \rho(\varphi)\boldsymbol{g}, \tag{4.2}$$

$$\mathrm{div}\,\boldsymbol{v} = 0, \tag{4.3}$$

$$\frac{\partial\varphi}{\partial t} + \boldsymbol{v}\cdot\nabla\varphi - \frac{1}{Pe}\mathrm{div}\left(\frac{m(\varphi)}{\rho(\varphi)}\nabla\left(\frac{\eta}{\rho(\varphi)}\right)\right) = 0, \tag{4.4}$$

$$\eta = \psi'(\varphi) - \alpha^2\Delta\varphi, \tag{4.5}$$

differs from (1), amongst other things, by the usage of the continuum surface tension force in its potential form: $\eta\,\nabla\varphi$. In equation (4), $\varepsilon = (\rho_1 - \rho_2)/\max(\rho_1, \rho_2)$ denotes the density contrast, $\varphi \in [-1, 1]$ is an order parameter, α is a dimensionless parameter related to the interface thickness, $\mathcal{K}$ is the capillarity coefficient, $\boldsymbol{g}$ is the gravitational force field, Pe is the Peclet number and $m(\varphi) = (1-\varphi^2)^2/(8\xi(\varphi))$ is the mobility coefficient, whereby $\xi(\varphi)$ denotes the alloy composition dependent friction coefficient. However, it is noteworthy to straighten that, unfortunately, neither global nor local energy inequalities are known for the model presented in (4). The same holds true for the model presented in (1) when the density ρ is not constant, making it difficult to conduct mathematical analysis.

Shen et al. [32] derived the following physically consistent phase field model for two-phase incompressible flows with variable density $\rho(\varphi) = \frac{\rho_1-\rho_2}{2}\varphi + \frac{\rho_1+\rho_2}{2}\varphi$ and viscosity $\mu(\varphi) = \frac{\mu_1-\mu_2}{2}\varphi + \frac{\mu_1+\mu_2}{2}\varphi$

$$\sigma(\sigma\boldsymbol{v})_t + \frac{1}{2}\nabla\cdot(\rho\boldsymbol{v})\boldsymbol{v} + (\rho\boldsymbol{v}\cdot\nabla)\,\boldsymbol{v} - \nabla\cdot 2\mu\boldsymbol{D}(\boldsymbol{v}) + \nabla p = -\lambda\nabla\cdot(\nabla\varphi\otimes\nabla\varphi)\,, \tag{5.1}$$

$$\nabla\cdot\boldsymbol{v} = 0, \tag{5.2}$$

$$\frac{\partial\varphi}{\partial t} + (\boldsymbol{v}\cdot\nabla)\,\varphi = -\gamma\Delta\left(\Delta\varphi - \psi'(\varphi)\right) \tag{5.3}$$

admitting the following energy law:

$$\frac{d}{dt}\int_\Omega\left(\frac{1}{2}|\sigma\boldsymbol{v}|^2 + \frac{\lambda}{2}|\nabla\varphi|^2 + \lambda\psi(\varphi)\right)\,\mathrm{d}\boldsymbol{x} = -\int_\Omega\left(\mu|\boldsymbol{D}(\boldsymbol{u})|^2 + \lambda\gamma|\nabla(\Delta\varphi - \psi'(\varphi))|^2\right)\,\mathrm{d}\boldsymbol{x} \tag{6}$$

In equation. (5), λ denotes the mixing energy density, γ is a diffusion parameter and $\sigma = \sqrt{\rho}$.

Abels et al. [1] recently derived a thermodynamically consistent generalization of (1.1)-(1.4) for the case of variable density based on a solenoidal velocity field $\boldsymbol{v}$. Their model, expressed through (7), fulfills local and global dissipation inequalities and is frame indifferent. Using the method of matched asymptotic expansions, that is, matching asymptotic expansions in the bulk region with expansions in the interfacial regions, various sharp interface models are derived in the limit when the interfacial thickness tends to zero ($\varepsilon \to 0$).

$$\begin{aligned}\partial_t(\rho(\varphi)\boldsymbol{v}) + \mathrm{div}\,(\rho(\varphi)\boldsymbol{v}\otimes\boldsymbol{v}) - \mathrm{div}\,(2\mu(\varphi)\boldsymbol{D}(\boldsymbol{v})) &= -\nabla p - \hat{\sigma}\varepsilon\mathrm{div}\,(\nabla\varphi\otimes\nabla\varphi)\\ &\quad - \mathrm{div}\left(\boldsymbol{v}\otimes\frac{\rho_1-\rho_2}{2}m(\varphi)\nabla\eta\right),\end{aligned} \tag{7.1}$$

$$\mathrm{div}\,\boldsymbol{v} = 0, \tag{7.2}$$

$$\partial_t\varphi + \boldsymbol{v}\cdot\nabla\varphi = \mathrm{div}\,(m(\varphi)\nabla\eta)\,, \tag{7.3}$$

$$\eta = \hat{\sigma}\varepsilon^{-1}\psi'(\varphi) - \hat{\sigma}\varepsilon\Delta\varphi \tag{7.4}$$

We conclude this section with a consolidated listing (see Table 1) of the models alongside their peculiarities. In conformity with the motivation and justification to present and elaborate on the essential features and shortcomings of the available models, this section and in particular Table 1 may greatly facilitate and accelerate the process of identifying a suitable model.

	Variable density $\rho(\varphi)$	Thermodynamically consistent	Admitting energy law	Sharp interface limit identifiable when $\varepsilon \to 0$
Model H		✓	✓	✓
Lowengrub et al.	✓	✓	✓	✓
Ding et al.	✓			✓
Boyer	✓			
Shen et al.	✓	✓	✓	
Abels et al.	✓	✓	✓	✓

Table 1: Traits of different phase field models for two-phase incompressible flows.

3. Mathematical model

Let $\Omega = (\Omega_1 \cup \Omega_2) \subset \mathbb{R}^n$ be an arbitrary open domain, with $n = 2$ or 3 and let its boundary $\partial\Omega$ be sufficiently smooth (e.g. Lipschitz continuous). Moreover, let Γ denote the interface between the different fluids or phases occupying the subdomains Ω_1 and Ω_2 and let $\boldsymbol{n}$ be the outward $(\Omega_1 \to \Omega_2)$ unit normal at the interface. Classical two-phase flow systems being based on models of surface tension forces either apply a force balance boundary condition

$$[\![-p\boldsymbol{I} + \mu\left(\nabla\boldsymbol{v} + (\nabla\boldsymbol{v})^T\right)]\!]\big|_\Gamma \cdot \boldsymbol{n} = \sigma\kappa\boldsymbol{n} \tag{8}$$

on the interface Γ or rewrite the internal force boundary condition as a volumetric surface tension force

$$\boldsymbol{f}_{st} = \sigma\kappa\boldsymbol{n}\delta(\Gamma, \boldsymbol{x}), \tag{9}$$

where σ is the surface tension coefficient, κ is the interface curvature and $\delta(\Gamma, \boldsymbol{x})$ is a Dirac delta function localizing the surface tension force to the interface.

Phase field methods on the other hand, are based on models of fluid free energy. The simplest free energy density model for isothermal fluids yielding two phases is

$$f(\varphi) = \frac{1}{2}\alpha|\nabla\varphi|^2 + \beta\psi(\varphi) \qquad \alpha > 0, \beta > 0 \tag{10}$$

and can be traced down to Van der Waals [38]. With φ denoting a measure of phase, the first term on the right hand side of (10) represents the interfacial (also known as "surface" or "gradient") free-energy density with a positive constant α. Having been introduced in the theory of phase transitions to model capillary effects and penalizing large gradients, it accounts for the fact that gradients in the concentration field φ are energetically unfavorable. The second part of the above expression involves a homogeneous (or "bulk") free-energy density function $\psi(\varphi)$ modeling the fluid components' immiscibility. It contains a term describing the entropy of mixing and a term taking into account the interaction between the two fluid components. The double-well function $\psi(\varphi)$ penalizes any mixing of the phases. A physically relevant expression for the potential ψ and $\varphi \in [-1, 1]$ is given by the logarithmic expression [5, 9]

$$\psi(\varphi) = T((1+\varphi)\log(1+\varphi) + (1-\varphi)\log(1-\varphi)) + T_c(1-\varphi^2), \tag{11}$$

where T and T_c are the temperature and the critical temperature of the mixture, respectively. For the phase separation phenomenon to occur, the relation between the temperatures need to satisfy $T < T_c$ such that $\psi(\varphi)$ is not convex and builds two minima corresponding to the two stable phases of the fluid (see Figure 1). In cases where T is close enough to T_c, expression (11) can be replaced

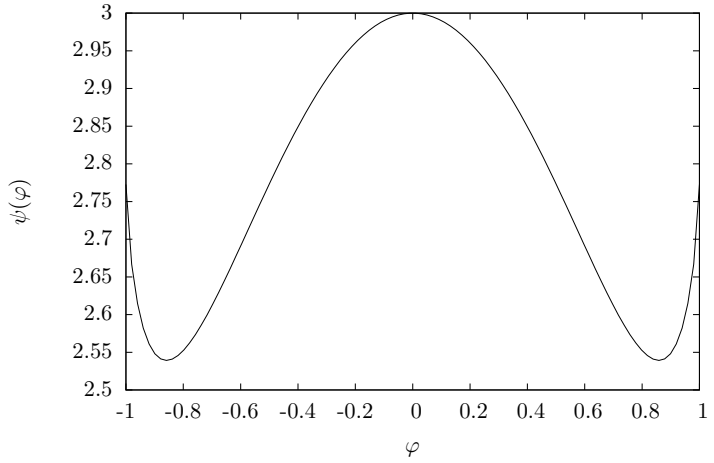

Figure 1: Homogeneous free energy density function (11) with $T = 2$ and $T_c = 3$.

by a polynomial approximation of the form $\psi(\varphi) = C_1\varphi^4 - C_2\varphi^2$. In fact all calculations in this paper were performed with

$$\psi(\varphi) = \frac{1}{4}(\varphi - 1)^2(\varphi + 1)^2, \tag{12}$$

where $\varphi \in [-1, 1]$ and $\varphi(x) = 1$ (respectively $\varphi(x) = -1$) if and only if fluid 1 (respectively fluid 2) is present at point x.

The theory of Cahn and Hilliard is based on Van der Waals' [38] hypothesis that equilibrium interface profiles are those that minimize a fluid free energy (Ginzburg-Landau free energy) functional

$$\mathcal{E}(\varphi) := \int_\Omega f \, \mathrm{d}\Omega = \int_\Omega \frac{1}{2}\alpha|\nabla\varphi|^2 + \beta\psi(\varphi) \, \mathrm{d}\Omega. \tag{13}$$

Variational calculus is used to determine the rate of change of the free energy functional $\mathcal{E}(\varphi)$ with respect to φ. More specifically, the variational derivative of $\mathcal{E}(\varphi)$ with respect to φ yields the chemical potential η being defined as

$$\eta = \frac{\delta\mathcal{E}}{\delta\varphi} = -\alpha\nabla^2\varphi + \beta\psi'(\varphi). \tag{14}$$

Equilibrium interface profiles satisfy

$$\beta\psi'(\varphi) - \alpha\nabla^2\varphi \equiv \eta = \text{const.}, \tag{15}$$

and setting α and β to respectively $O(\epsilon)$ and $O(1/\epsilon)$, produces phase field interfaces of thickness $O(\epsilon)$ and surface tension $O(1)$. Cahn and Hilliard generalized the problem to a mass diffusion equation in a binary system applying the principle of conservation of mass with a local diffusion mass flux $\boldsymbol{J}$ that is specified in terms of the chemical potential. The constitutive equation for the flux sets it proportional to the negative of the chemical potential, for the transport takes place from

locations with a high chemical potential to those with a lower one. Therefore, we have the following definition for the flux

$$\boldsymbol{J} = -m(\varphi)\nabla\eta, \tag{16}$$

where $m(\varphi)$ is a concentration dependent mobility function[1] and is often replaced by a constant for simplification reasons. However, for all the calculations in this article we have used the following nonlinear mobility function

$$m(\varphi) = D(\varphi^2 - 1)^2, \tag{17}$$

where D represents a scaling parameter. In the absence of sources and sinks, mass conservation for φ requires

$$\frac{d\varphi}{dt} + \nabla \cdot \boldsymbol{J} = \frac{\partial\varphi}{\partial t} + \nabla \cdot (\boldsymbol{v}\varphi) + \nabla \cdot \boldsymbol{J} = 0. \tag{18}$$

Above, $\boldsymbol{v}$ denotes an advective velocity field. Requiring it to be solenoidal, that is, $\nabla \cdot \boldsymbol{v} = 0$ and substituting expressions (16) and (17) into (18), yields the fourth order advective Cahn–Hilliard equation

$$\frac{\partial\varphi}{\partial t} + \boldsymbol{v} \cdot \nabla\varphi = \nabla \cdot (m(\varphi)\nabla\eta) = \nabla \cdot \left(m(\varphi)\nabla\left(-\alpha\nabla^2\varphi + \beta\psi'(\varphi)\right)\right). \tag{19}$$

Ignoring the advective term $\boldsymbol{v} \cdot \nabla\varphi$, the pure Cahn–Hilliard equation approximates interfacial diffusion fluxes as being proportional to chemical potential gradients and governs the creation, movement and decomposition of diffusively controlled interfaces. Finally, the following boundary conditions are required at $\partial\Omega$ to complete the system

$$\begin{aligned} &\nabla\eta \cdot \boldsymbol{n} = 0, \quad \text{(no flux)} \\ &\nabla\varphi \cdot \boldsymbol{n} = \frac{1}{\epsilon\sqrt{2}}\cos(\theta)(1-\varphi^2), \quad \text{(contact angle)} \end{aligned} \tag{20}$$

where θ is an equilibrium contact angle[2] between the interface Γ and $\partial\Omega$. All computations in this article were performed with $\theta = \pi/2$, implying $\nabla\varphi \cdot \boldsymbol{n} = 0$, and hence an interface orthogonal to the boundary of the computational domain.

Recalling equation (15) and using the free energy density function (12), the equilibrium interface profile is given by the solution of the equation

$$\eta(\varphi) = -\alpha\nabla^2\varphi + \beta\psi'(\varphi) = -\alpha\Delta\varphi + \beta\varphi(\varphi^2 - 1) = 0. \tag{21}$$

The solution is characterized by two stable minima at $\varphi \approx \pm 1$ standing for the two phases and a one-dimensional transition region given by

$$\varphi(x) = \tanh\left(\frac{x}{\sqrt{2}\sqrt{\alpha/\beta}}\right). \tag{22}$$

Following Jacqmin [24], the surface tension of the interface of an isothermal fluid system in equilibrium is equal to the integral of the free energy density through the interface. Therefore, recalling that the first term $(\alpha|\nabla\varphi|^2)$ of (10) is referred to the interfacial or surface free-energy density, the surface tension of a plane phase field interface is given by

$$\sigma = \alpha\int_{-\infty}^{\infty}\left(\frac{d\varphi}{dx}\right)^2 \mathrm{d}\boldsymbol{x} = \frac{2\sqrt{2}}{3}\sqrt{\alpha\beta}. \tag{23}$$

[1] In general tensor-valued mobility functions are consistent with the Cahn-Hilliard equation.

[2] For an interface in equilibrium, a contact angle condition $cos(\theta) = \frac{\sigma_{2S} - \sigma_{1S}}{\sigma}$ (Young's law) may be posed, where θ is the equilibrium contact angle and σ_{iS} is the interfacial energy between the solid and component i. The contact angle characterizes the wettability of the surface with $\theta = 0$ denoting complete wetting.

Since for general ψ, the surface tension and equilibrium interface thickness behave as $\sigma \propto \sqrt{\alpha\beta}$ and $\epsilon \propto \sqrt{\alpha/\beta}$, respectively [24], identity (23) is satisfied with the introduction of an auxiliary interface thickness $\xi = \sqrt{\alpha/\beta}$ and the following settings for the parameters α and β:

$$\alpha = \frac{3}{2\sqrt{2}}\sigma\xi, \qquad \beta = \frac{3}{2\sqrt{2}}\frac{\sigma}{\xi}. \tag{24}$$

The advective Cahn-Hilliard equation (19) is a stiff and nonlinear partial differential equation characterized by the presence of fourth-order spatial derivatives. Its finite element discretization in terms of primal variational formulation requires piecewise smooth and globally $\mathcal{C}^1$ continuous basis functions constituting high demands on discrete approximation spaces. In fact, the number of $\mathcal{C}^1$ finite elements being applicable to complex geometries is already very limited in two dimensions [18, 34]. Albeit Isogeometric Analysis easily allows the setup of high order discrete approximation spaces, we use the mixed formulation (25) of the Cahn–Hilliard equation, taking the chemical potential η as an auxiliary variable.

$$\begin{aligned} \frac{\partial\varphi}{\partial t} + \boldsymbol{v}\cdot\nabla\varphi - \nabla\cdot(m(\varphi)\nabla\eta) &= 0, \\ \eta - \beta\,\frac{d\psi(\varphi)}{d\varphi} + \alpha\,\nabla^2\varphi &= 0. \end{aligned} \tag{25}$$

Since the highest spatial derivatives appearing in the mixed formulation are reduced to order two, standard $\mathcal{C}^0$ discretizations may be used that avoid the costs associated with the usage of high-order and high-continuity basis functions. Besides, using (25) we avoid complications with the imposition of nonlinear boundary conditions arising from the discretization of the mass flux in the primal form.

In the sequel we focus on the coupling aspects of the diffuse interface model with a flow model for two incompressible, immiscible and isothermal fluids of different mass densities ρ_1, ρ_2 and viscosities μ_1, μ_2. We let the volume fraction of the first fluid in the mixture be defined as

$$\vartheta = \frac{dV_1}{dV}, \tag{26}$$

where dV_1 is the volume filled by fluid 1 and we use the following rescaling

$$\varphi = 2\vartheta - 1 \tag{27}$$

of the order parameter ϑ to the range $[-1, 1]$ to determine the composition of the two components in a volume element of the domain. Then, the total density and viscosity of the mixture is given as the volume averaged sum of each component‘s respective contribution, that is,

$$\begin{aligned} \rho(\varphi(x,y)) &= \rho_1(1+\varphi)/2 + \rho_2(1-\varphi)/2, \\ \mu(\varphi(x,y)) &= \mu_1(1+\varphi)/2 + \mu_2(1-\varphi)/2. \end{aligned} \tag{28}$$

Eventually, the Navier–Stokes–Cahn–Hilliard variable density, variable viscosity incompressible two-phase flow model (29) is obtained by the extension of the Navier–Stokes equations with a surface tension force term $\eta\nabla\varphi$, written in its potential form, and a fluid induced transport term $\boldsymbol{v}\cdot\nabla\varphi$ in

the Cahn-Hilliard equation.

$$\rho(\varphi)\left(\frac{\partial \boldsymbol{v}}{\partial t}+(\boldsymbol{v}\cdot\nabla)\boldsymbol{v}\right)-\nabla\cdot\left(\mu(\varphi)\left(\nabla\boldsymbol{v}+(\nabla\boldsymbol{v})^T\right)\right)=-\nabla p+\rho(\varphi)\boldsymbol{g}+\eta\nabla\varphi \text{ in } \Omega_T, \tag{29.1}$$

$$\nabla\cdot\boldsymbol{v}=0 \qquad \text{in } \Omega_T, \tag{29.2}$$

$$\frac{\partial\varphi}{\partial t}+\boldsymbol{v}\cdot\nabla\varphi-\nabla\cdot(m(\varphi)\nabla\eta)=0 \qquad \text{in } \Omega_T, \tag{29.3}$$

$$\eta-\beta\,\frac{d\psi(\varphi)}{d\varphi}+\alpha\,\nabla^2\varphi=0 \qquad \text{in } \Omega_T, \tag{29.4}$$

$$\varphi(\boldsymbol{x},0)=\varphi_0(\boldsymbol{x}),\quad \boldsymbol{v}(\boldsymbol{x},0)=\boldsymbol{v}_0(\boldsymbol{x}) \qquad \text{in } \Omega, \tag{29.5}$$

$$\frac{\partial\varphi}{\partial\boldsymbol{n}}=\frac{\partial\eta}{\partial\boldsymbol{n}}=0,\quad \boldsymbol{v}=\boldsymbol{v}_D \qquad \text{on } (\partial\Omega_T)_D, \tag{29.6}$$

$$\left(-p\boldsymbol{I}+\mu(\varphi)\left(\nabla\boldsymbol{v}+(\nabla\boldsymbol{v})^T\right)\right)\cdot\boldsymbol{n}=\boldsymbol{t} \qquad \text{on } (\partial\Omega_T)_N \tag{29.7}$$

Above, $\Omega_T=\Omega\times(0,T)$, $(\partial\Omega)_D$ is the Dirichlet part of the domain boundary, $\boldsymbol{t}$ is the prescribed traction force on the Neumann boundary $(\partial\Omega)_N$, $\boldsymbol{g}$ is the gravitational force field and p is the pressure variable acting as a Lagrange multiplier in the course of enforcing the incompressibility condition. This basically corresponds to the model presented by Ding et al. [10] which can be seen as a generalization of Model H (see equation (1)) for the case of different densities and viscosities. In contrast to Model H, a surface tension force term in potential form $\eta\nabla\varphi$ has replaced the divergence of the phase induced stress tensor $-\hat{\sigma}\varepsilon\,(\nabla\varphi\otimes\nabla\varphi)$. The latter, that is, $-\hat{\sigma}\varepsilon\,\mathrm{div}\,(\nabla\varphi\otimes\nabla\varphi)$, represents the phase induced force.

4. Discretization with Isogeometric finite elements

We use Isogeometric Analysis for the approximation of the solution of the coupled equation system (29). Inspired by operator splitting techniques, it is solved in two consecutive stages in order to alleviate numerical treatment. More specifically, given a flow field $\boldsymbol{v}$, we first solve the phase field equations (29.3,29.4) in order to update the phase φ and chemical potential information η. The second step eventually uses these information to compute the surface tension force and the phase dependent values of density $\rho(\varphi(\boldsymbol{x}))$ and viscosity $\mu(\varphi(\boldsymbol{x}))$ in the course of the solution of the Navier–Stokes equations (29.1,29.2). As time integrator for both systems, we use the one-step θ-scheme with $\theta=1$ or $\theta=0.5$ respectively yielding the 1st order implicit Euler or 2nd order Crank-Nicolson scheme. For the approximation of the velocity and pressure functions in the Navier–Stokes equations, we use LBB-stable Taylor–Hood-like B-spline/NURBS[3] space pairs $\hat{\mathbf{V}}_h^{TH}/\hat{Q}_h^{TH}$ which are defined in the parametric spline domain $\hat{\Omega}$ as

$$\begin{aligned}\hat{\mathbf{V}}_h^{TH}&\equiv\hat{\mathbf{V}}_h^{TH}(\mathbf{p},\boldsymbol{\alpha})=\boldsymbol{\mathcal{N}}_{\alpha_1,\alpha_2}^{p_1+1,p_2+1}=\mathcal{N}_{\alpha_1,\alpha_2}^{p_1+1,p_2+1}\times\mathcal{N}_{\alpha_1,\alpha_2}^{p_1+1,p_2+1},\\ \hat{Q}_h^{TH}&\equiv\hat{Q}_h^{TH}(\mathbf{p},\boldsymbol{\alpha})=\mathcal{N}_{\alpha_1,\alpha_2}^{p_1,p_2}.\end{aligned} \tag{30}$$

Above, $\mathcal{N}_{\alpha_1,\alpha_2}^{p_1+1,p_2+1}$ denotes a tensor product bivariate NURBS space of polynomial degrees p_i+1 and continuities α_i, $i=1,2$, with respect to parametric spline domain directions ξ_i. We refer to Hosseini et al. [21] for a detailed description of the above spline spaces. In all performed computations we used a $\mathcal{C}^0$ $\boldsymbol{\mathcal{N}}_{0,0}^{2,2}/\mathcal{N}_{0,0}^{1,1}$ NURBS space pair for the approximation of the velocity and pressure functions. This corresponds to the Isogeometric counterpart of a Q_2Q_1 Taylor–Hood space well known from the finite element literature. The degree and continuity of the discrete spaces used for

[3] Non-Uniform Rational B-splines (NURBS)

the approximation of the Navier–Stokes velocity and Cahn–Hilliard phase and chemical potential functions are set to be identical. In the sequel we picture the individual solution stages and outline the spatial and temporal discretization of the involved equations.

Step 1 – Cahn–Hilliard equation:
For the treatment of nonlinearity in the advective Cahn–Hilliard equation, we seek for the current approximation of the solution $u^k = (\varphi^k, \eta^k)$ small perturbations $\delta u = (\delta\varphi, \delta\eta)$, such that

$$\begin{aligned} \varphi^{k+1} &= \varphi^k + \delta\varphi, \\ \eta^{k+1} &= \eta^k + \delta\eta \end{aligned} \tag{31}$$

satisfy the nonlinear partial differential equation (25). Under the premise that $\delta\varphi$ is sufficiently small, we linearize the nonlinear function $\psi'(\varphi)$ as:

$$\psi'(\varphi^{k+1}) = \psi'(\varphi^k) + \psi''(\varphi^k)\,\delta\varphi + \mathcal{O}((\delta\varphi)^2) \approx \psi'(\varphi^k) + \psi''(\varphi^k)\,\delta\varphi. \tag{32}$$

After the time discretization with the θ-scheme, we arrive at

$$\begin{aligned} \frac{\varphi^{n+1}-\varphi^n}{\Delta t} + \theta\left((\boldsymbol{v}\cdot\nabla)\varphi^{n+1} - \nabla\cdot m\,\nabla\eta^{n+1}\right) + (1-\theta)\left((\boldsymbol{v}\cdot\nabla)\varphi^{n} - \nabla\cdot m\,\nabla\eta^{n}\right) = 0 \quad &\text{in } \Omega_T, \\ \eta^{n+1} - \beta\,\psi'(\varphi^{n+1}) + \alpha\nabla^2\varphi^{n+1} = 0 \quad &\text{in } \Omega_T, \end{aligned} \tag{33}$$

where the boundary terms have not been displayed for the sake of lucidity. Above, in the spirit of Picard iteration, the nonlinear mobility function $m(\varphi)$ is evaluated with respect to the already available values of the phase field, that is, φ^n. This linearization allows it to be treated as a constant and simplifies the numerical treatment.

The variational form of the problem reads: Find $\varphi(\boldsymbol{x},t)$ and $\eta(\boldsymbol{x},t) \in \mathcal{H}^1(\Omega)\times(0,T)$, such that $\forall q, v \in \mathcal{H}^1_0(\Omega)$ it holds:

$$\begin{aligned} &\int_\Omega \frac{\varphi^{n+1}-\varphi^n}{\Delta t}\,q\,\mathrm{d}\boldsymbol{x} + \theta\left(\int_\Omega (\boldsymbol{v}\cdot\nabla)\varphi^{n+1}\,q + m\,\nabla\eta^{n+1}\cdot\nabla q\,\mathrm{d}\boldsymbol{x} - \int_{\partial\Omega}\boldsymbol{n}\cdot m\,\nabla\eta^{n+1}\,q\,ds\right) \\ &\qquad +(1-\theta)\left(\int_\Omega (\boldsymbol{v}\cdot\nabla)\varphi^{n}\,q + m\,\nabla\eta^{n}\cdot\nabla q\,\mathrm{d}\boldsymbol{x} - \int_{\partial\Omega}\boldsymbol{n}\cdot m\,\nabla\eta^{n}\,q\,ds\right) = 0, \\ &\int_\Omega \eta^{n+1}\,v\,\mathrm{d}\boldsymbol{x} - \int_\Omega \beta\,\frac{d\psi(\varphi^{n+1})}{d\varphi}\,v\,\mathrm{d}\boldsymbol{x} - \int_\Omega \alpha\,\nabla\varphi^{n+1}\cdot\nabla v\,\mathrm{d}\boldsymbol{x} + \int_{\partial\Omega}\boldsymbol{n}\cdot\alpha\nabla\varphi^{n+1}\,ds = 0. \end{aligned} \tag{34}$$

The application of (31) and (32) on (34) yields:

$$\begin{aligned} &\int_\Omega (\varphi^k + \delta\varphi - \varphi^n)\,q\,\mathrm{d}\boldsymbol{x} + \theta\Delta t\int_\Omega (\boldsymbol{v}\cdot\nabla)(\varphi^k+\delta\varphi)\,q + m\,\nabla(\eta^k+\delta\eta)\cdot\nabla q\,\mathrm{d}\boldsymbol{x} \\ &\qquad +(1-\theta)\Delta t\int_\Omega (\boldsymbol{v}\cdot\nabla)\varphi^n\,q + m\,\nabla\eta^n\cdot\nabla q\,\mathrm{d}\boldsymbol{x} = 0, \\ &\int_\Omega (\eta^k+\delta\eta)\,v\,\mathrm{d}\boldsymbol{x} - \int_\Omega \beta\,\left(\psi'(\varphi^k) + \psi''(\varphi^k)\,\delta\varphi\right)\,v\,\mathrm{d}\boldsymbol{x} - \int_\Omega \alpha\,\nabla(\varphi^k+\delta\varphi)\cdot\nabla v\,\mathrm{d}\boldsymbol{x} = 0. \end{aligned} \tag{35}$$

In equation (35), the indices n and k refer to the solution from the last time step and the current Newton-iterate, respectively. $(\delta\varphi, \delta\eta)$ is associated to the Newton-update.
Gathering all terms with the unknowns $\delta\varphi$ and $\delta\eta$ on the left hand side, we obtain the following

expressions

$$
\begin{aligned}
&\int_\Omega \underbrace{\delta\varphi\, q}_{\mathbf{M}} + \theta\Delta t \left(\underbrace{(\boldsymbol{v}\cdot\nabla)\delta\varphi\, q}_{\mathbf{C}} + m \underbrace{\nabla\delta\eta\cdot\nabla q}_{\mathbf{D}} \right) \,\mathrm{d}\boldsymbol{x} = \\
&\int_\Omega -\underbrace{\varphi^k\, q}_{\mathbf{M}} - \theta\Delta t \left(\underbrace{(\boldsymbol{v}\cdot\nabla)\varphi^k\, q}_{\mathbf{C}} + m \underbrace{\nabla\eta^k\cdot\nabla q}_{\mathbf{D}} \right) \,\mathrm{d}\boldsymbol{x} \\
&+ \int_\Omega \underbrace{\varphi^n\, q}_{\mathbf{M}} - (1-\theta)\Delta t \left(\underbrace{(\boldsymbol{v}\cdot\nabla)\varphi^n\, q}_{\mathbf{C}} + m \underbrace{\nabla\eta^n\cdot\nabla q}_{\mathbf{D}} \right) \,\mathrm{d}\boldsymbol{x}, \\
&\int_\Omega \underbrace{\delta\eta\, v}_{\mathbf{M}} \,\mathrm{d}\boldsymbol{x} - \int_\Omega \beta\, \underbrace{\psi''(\varphi^k)\,\delta\varphi\, v}_{\mathbf{N}} \,\mathrm{d}\boldsymbol{x} - \int_\Omega \alpha\, \underbrace{\nabla\delta\varphi\cdot\nabla v}_{\mathbf{D}} \,\mathrm{d}\boldsymbol{x} = \\
&- \int_\Omega \underbrace{\eta^k\, v}_{\mathbf{M}} \,\mathrm{d}\boldsymbol{x} + \int_\Omega \beta\, \underbrace{\psi'(\varphi^k)\, v}_{\mathbf{n}} \,\mathrm{d}\boldsymbol{x} + \int_\Omega \alpha \underbrace{\nabla\varphi^k\cdot\nabla v}_{\mathbf{D}} \,\mathrm{d}\boldsymbol{x}.
\end{aligned}
\tag{36}
$$

The corresponding discrete system for the Newton-Iteration may now be written in matrix form as

$$
\begin{matrix} q \\ v \end{matrix} \underbrace{\begin{pmatrix} \mathbf{M}+\theta\Delta t\mathbf{C} & \theta\Delta t m\mathbf{D} \\ -\alpha\mathbf{D}-\beta\mathbf{N} & \mathbf{M} \end{pmatrix}}_{\mathbf{J}} \begin{pmatrix} \delta\varphi \\ \delta\eta \end{pmatrix} = \underbrace{\begin{pmatrix} -\mathbf{M}-\theta\Delta t\mathbf{C} & -\theta\Delta t m\mathbf{D} \\ \alpha\mathbf{D} & -\mathbf{M} \end{pmatrix} \begin{pmatrix} \varphi^k \\ \eta^k \end{pmatrix} + \begin{pmatrix} \mathbf{0} \\ \beta\mathbf{n} \end{pmatrix} + \begin{pmatrix} \mathbf{M}-(1-\theta)\Delta t\mathbf{C} & -(1-\theta)\Delta t m\mathbf{D} \\ \mathbf{0} & \mathbf{0} \end{pmatrix} \begin{pmatrix} \varphi^n \\ \eta^n \end{pmatrix}}_{-\mathbf{F}}
\tag{37}
$$

and solved for δu in order to update the unknowns as $(\varphi^{k+1}, \eta^{k+1}) = (\varphi^k, \eta^k) + (\delta\varphi^k, \delta\eta^k)$.

Step 2 – Navier–Stokes equations: This step involves the numerical approximation of the solution of the unsteady variable density and variable viscosity Navier–Stokes equations extended by a surface tension force term. The initial condition is required to satisfy $\nabla\cdot\boldsymbol{v}_0 = 0$. With $\boldsymbol{b}$ denoting the body force term, the variational formulation of the problems (29.1,29.2) reads: Find $\boldsymbol{v}(\boldsymbol{x},t) \in \boldsymbol{\mathcal{H}}_0^1(\Omega)\times(0,T)$ and $p(\boldsymbol{x},t) \in \mathcal{L}_2(\Omega)/\mathbb{R}\times(0,T)$, such that for all $(\boldsymbol{w},q) \in \boldsymbol{\mathcal{H}}_0^1(\Omega)\times\mathcal{L}_2(\Omega)/\mathbb{R}$ it holds

$$
\begin{cases} (\boldsymbol{w},\boldsymbol{v}_t) + a(\boldsymbol{w},\boldsymbol{v}) + c(\boldsymbol{v};\boldsymbol{w},\boldsymbol{v}) + b(\boldsymbol{w},p) = (\boldsymbol{w},\boldsymbol{b}) + (\boldsymbol{w},\boldsymbol{t})_{(\partial\Omega)_N} \\ b(q,\boldsymbol{v}) = 0. \end{cases}
\tag{38}
$$

Replacement of the linear-, bilinear- and trilinear forms with their respective definitions and application of integration by parts yields

$$
\begin{aligned}
&\underbrace{\int_\Omega \rho(\varphi)\boldsymbol{w}\cdot\boldsymbol{v}_t \,\mathrm{d}\Omega}_{(\boldsymbol{w},\boldsymbol{v}_t)} + \underbrace{\int_\Omega \mu(\varphi)\nabla\boldsymbol{w} \,:\, \left(\nabla\boldsymbol{v} + (\nabla\boldsymbol{v})^T\right) \,\mathrm{d}\Omega}_{a(\boldsymbol{w},\boldsymbol{v})} + \underbrace{\int_\Omega \rho(\varphi)\boldsymbol{w}\cdot\boldsymbol{v}\cdot\nabla\boldsymbol{v} \,\mathrm{d}\Omega}_{c(\boldsymbol{v};\boldsymbol{w},\boldsymbol{v})} = \\
&\underbrace{\int_\Omega \nabla\cdot\boldsymbol{w}\, p \,\mathrm{d}\Omega}_{b(\boldsymbol{w},p)} - \underbrace{\int_\Omega q\,\nabla\cdot\boldsymbol{v} \,\mathrm{d}\Omega}_{b(q,\boldsymbol{v})} + \underbrace{\int_\Omega \rho(\varphi)\boldsymbol{w}\cdot\boldsymbol{b} + \boldsymbol{w}\cdot\eta\nabla\varphi \,\mathrm{d}\Omega}_{(\boldsymbol{w},\boldsymbol{b})} + \\
&\underbrace{\int_{(\partial\Omega)_N} \mu(\varphi)\,\boldsymbol{w}\cdot\left(\left(\nabla\boldsymbol{v} + (\nabla\boldsymbol{v})^T\right)\cdot\boldsymbol{n}\right) \,\mathrm{d}(\partial\Omega)_N - \int_{(\partial\Omega)_N} \boldsymbol{w}\cdot\boldsymbol{n}\, p \,\mathrm{d}(\partial\Omega)_N}_{(\boldsymbol{w},\boldsymbol{t})_{(\partial\Omega)_N}}.
\end{aligned}
\tag{39}
$$

A downcast of the variational formulation (38) to the discrete level gives rise to the problem statement

$$\begin{cases} \text{Find } \boldsymbol{v}^h \in \boldsymbol{\mathcal{H}}_0^1(\Omega) \cap \mathbf{V}_h^{TH} \times (0,T) \text{ and } p^h \in \mathcal{L}_2(\Omega)/\mathbb{R} \cap Q_h^{TH} \times (0,T), \text{such that} \\ \forall (\boldsymbol{w}^h, q^h) \in \boldsymbol{\mathcal{H}}_0^1(\Omega) \cap \mathbf{V}_h^{TH} \times \mathcal{L}_2(\Omega)/\mathbb{R} \cap Q_h^{TH} \\ (\boldsymbol{w}^h, \boldsymbol{v}_t^h) + a(\boldsymbol{w}^h, \boldsymbol{v}^h) + c(\boldsymbol{v}^h; \boldsymbol{w}^h, \boldsymbol{v}^h) + b(\boldsymbol{w}^h, p^h) = (\boldsymbol{w}^h, \boldsymbol{b}^h) + (\boldsymbol{w}^h, \boldsymbol{t}^h)_{(\partial\Omega)_N} \\ b(q^h, \boldsymbol{v}^h) = 0, \end{cases} \tag{40}$$

with superscript h dubbing the mesh family index. Using Isogeometric Taylor-Hood finite elements and the θ-scheme for the respective discretizations in space and time, the following discrete system

$$\begin{aligned} &\underbrace{\begin{pmatrix} \frac{1}{\Delta t}\mathbf{M}(\varphi^{n+1}) + \theta(\mathbf{D}(\varphi^{n+1}) + \mathbf{C}(v^{n+1}, \varphi^{n+1})) & \mathbf{G} \\ \mathbf{G}^T & \mathbf{0} \end{pmatrix}}_{\mathbf{S}_l} \underbrace{\begin{pmatrix} \mathbf{v}^{n+1} \\ \mathbf{p}^{n+1} \end{pmatrix}}_{\mathbf{u}^{n+1}} = \\ &\underbrace{\begin{pmatrix} \frac{1}{\Delta t}\mathbf{M}(\varphi^n) - (1-\theta)(\mathbf{D}(\varphi^n) + \mathbf{C}(v^n, \varphi^n)) & \mathbf{0} \\ \mathbf{0} & \mathbf{0} \end{pmatrix}}_{\mathbf{S}_r} \underbrace{\begin{pmatrix} \mathbf{v}^n \\ \mathbf{p}^n \end{pmatrix}}_{\mathbf{u}^n} + \underbrace{\theta\, \mathbf{f}^{n+1}(\eta^{n+1}, \varphi^{n+1})}_{\mathbf{b}^{n+1}} + \underbrace{(1-\theta)\mathbf{f}^n(\eta^n, \varphi^n)}_{\mathbf{b}^n} \end{aligned} \tag{41}$$

is obtained, where $\mathbf{M}, \mathbf{D}, \mathbf{C}, \mathbf{G}$, and $\mathbf{G^T}$ denote the mass, rate of deformation, advection, gradient, and divergence matrices, respectively. The body and the surface tension force terms are discretized altogether into $\mathbf{f}$. For the treatment of the nonlinearity in the Navier–Stokes equations (29.1,29.2), we use a Newton-Iteration

$$\mathbf{J}(\mathbf{u}^k, \varphi^k)\, \delta\mathbf{u} = -\mathbf{F}(\mathbf{u}^k, \mathbf{u}^n, \eta^k, \eta^n, \varphi^k, \varphi^n) \tag{42.1}$$

$$\mathbf{u}^{k+1} = \mathbf{u}^k + \delta\mathbf{u}, \tag{42.2}$$

whose right hand side is set to be the residual of equation (41), that is,

$$\mathbf{F}(\mathbf{u}^{n+1}, \mathbf{u}^n, \eta^{n+1}, \eta^n, \varphi^{n+1}, \varphi^n) = \mathbf{S}_l\, \mathbf{u}^{n+1} - \mathbf{S}_r\, \mathbf{u}^n - \mathbf{b}^{n+1} - \mathbf{b}^n. \tag{43}$$

For a detailed description of the setup of the Jacobian $\mathbf{J}$ in equation (42), we refer to [21].

5. Numerical results

Three numerical experiments are performed to assess the results obtained from the application of Isogeometric Analysis to two-phase flow problems. As aforementioned, the static bubble in equilibrium, the rising bubble and the Rayleigh–Taylor instability two-phase flow problems serve as model problems, each discussed in a separate section (5.1,5.2,5.3). Special emphasis is put on the rising bubble flow scenario whose setup follows an official two-phase flow benchmark problem and for which there exists an extensive set of results computed with different approximation methods by different research groups.

5.1. Static bubble

Being a simple setup, yet exhibiting prototypical behavior for multiphase flows, we consider a stationary bubble at equilibrium. This setup holds e.g. for the slow motion of a gas bubble in a viscoplastic fluid as described in [11]. With the bubble being at rest, the velocity field in the computational domain is expected to be zero. Nevertheless, numerical approximations of the velocity field unfortunately produce spurious currents, as for instance reported in [14, 33]. The computed pressure field is expected to satisfy the Laplace-Young law

$$p_i = p_o + \sigma/r, \tag{44}$$

where r is the bubble radius, σ is the surface tension coefficient and p_i and p_o denote the pressure inside ($x = 0.5, y = 0.5$) and outside ($x = 1.0, y = 0.5$) of the bubble, respectively. We set our computational domain Ω to be the unit square and partition it to two disjoint areas Ω_1 and Ω_2, such that $\Omega = \Omega_1 \cup \Omega_2$. Then, the static bubble is represented by the domain Ω_2 which is set up to be a circle of radius $r = 1/4$, centered at position $(1/2, 1/2)$. In order to setup the initial phase field profile, we perform a finite element L^2–projection

$$\int_\Omega (f - P_h f)\, w \, \mathrm{d}\boldsymbol{x} = 0, \quad \forall w \in \mathcal{W}_h \tag{45}$$

of the profile

$$f = \varphi_{\text{bubble}}(\boldsymbol{x}) = \begin{cases} +1, & \text{for } \boldsymbol{x} \in \Omega_1 \\ -1, & \text{for } \boldsymbol{x} \in \Omega_2 \end{cases} \tag{46}$$

on the NURBS-space degrees of freedom associated with the phase variable, whereby $\mathcal{W}_h$ denotes a suitable discrete space of weighting/test functions.

The gravitational force is neglected and the densities and viscosities of both fluids as well as the surface tension coefficient are set to 1. We use no-slip velocity boundary conditions in the entire domain and fix the value of the discrete pressure field at the lower left domain node with $p = 0$. Table 2 illustrates our pressure and velocity results for the above choice of parameters. Starting off

$\mathrm{N_{el}}$	h	ξ	p_i	p_o	$\lvert\Delta p - (\frac{\sigma}{r})\rvert/(\frac{\sigma}{r})$	$\lvert p_i - p_o\rvert/(\frac{\sigma}{r})$	$\lVert p - p_h\rVert_{L^2}$	$\lVert \boldsymbol{v} - \boldsymbol{v_h}\rVert_{L^2}$
256	2^{-4}	0.0400	4.05234	-0.00431	0.01416	1.01416	0.539996	2.27e-04
1024	2^{-5}	0.0200	3.99563	-0.00233	0.00051	0.99949	0.379967	6.67e-05
4096	2^{-6}	0.0125	4.00642	-0.00139	0.00195	1.00195	0.296332	6.77e-05
16384	2^{-7}	0.007125	4.00067	-0.00074	0.00035	1.00035	0.222107	1.28e-04

Table 2: Pressure and velocity errors for surface tension coefficient $\sigma = 1$ and bubble radius $r = 1/4$.

with the pressure jump $[\![p]\!] = |p_i - p_o|$ across the interface, it is shown to converge to the value 4, corresponding to the output of the Laplace-Young law for the above parametrization. Moreover, the precision and convergence of both the spurious velocity errors and the pressure difference are in good agreement with the sharp interface model results at our disposal, as for instance [37]. We refer to Figure 2 for a graphical representation of the pressure and velocity profiles. The spurious velocities are shown to build pairwise counter rotating vortices at the phase boundary with the impression of attempting to tear the fluid-fluid interface. The pressure field expectedly exhibits a rapid, yet smooth transition in the interface layer. As illustrated in Figure 3 (left), a lateral view of the pressure profile for different mesh refinement levels and diffuse interface widths reveals the convergence of the shape to a reference cylinder with radius $r = 1/4$ and height $1/r$. We conclude the static bubble test case with the investigation of the pressure jumps for the following choice of bubble radii $r = 1/8,\ 1/4,\ 3/8,\ 7/16$, where the results - displayed to the right of Figure 3 - are shown to tightly integrate with the Laplace-Young law.

5.2. Rising bubble

The rising bubble benchmark considers two initially quiescent fluids with different densities and viscosities in a rectangular domain $\Omega = \Omega_1 \cup \Omega_2 = (0, 1) \times (0, 2)$, where fluid i occupies the subdomain Ω_i. The lighter liquid (bubble) represented by the initially circular area Ω_2 with radius $r = 1/4$ and center $c = (1/2, 1/2)$ is subject to rising due to the effects of buoyancy. At the top and bottom boundaries we use the no-slip ($\boldsymbol{v} = 0$) boundary condition, whereas the free slip ($\boldsymbol{v} \cdot \boldsymbol{n} = 0, \boldsymbol{\tau} \cdot \left(\nabla \boldsymbol{u} + (\nabla \boldsymbol{u})^T\right) \cdot \boldsymbol{n} = 0, \boldsymbol{\tau} :=$ tangent vector) boundary condition is imposed on the

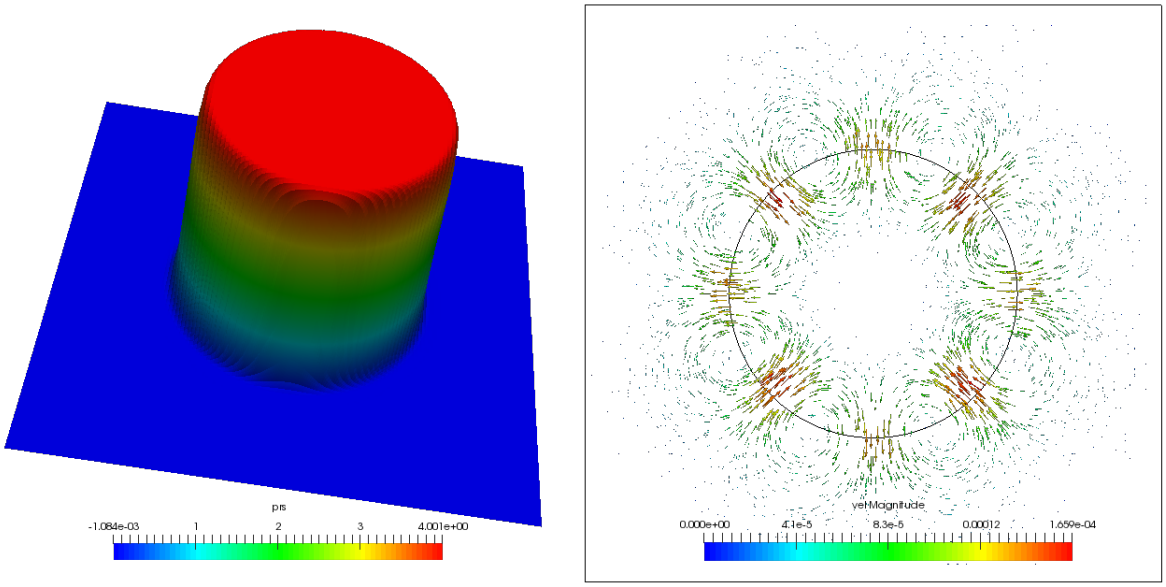

Figure 2: Pressure and velocity profiles for surface tension coefficient $\sigma = 1$ and bubble radius $r = 1/4$.

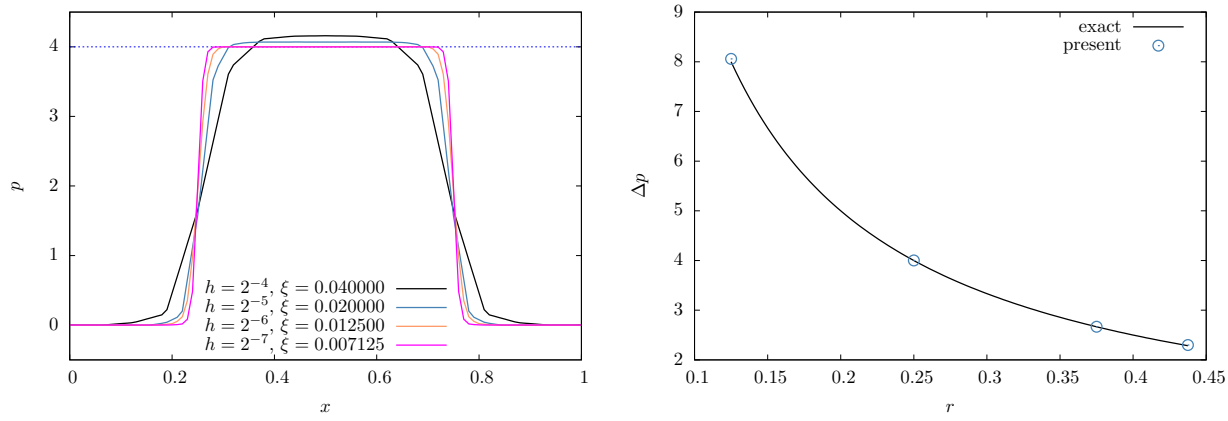

Figure 3: Left: Static bubble pressure profile development for surface tension coefficient $\sigma = 1$ and bubble radius $r = 1/4$. Right: Pressure differences Δp for a set of different bubble radii r compared to exact results based on the Laplace-Young law (44).

vertical walls. This setup, graphically represented by Figure 4, corresponds to the FeatFlow[4] rising bubble benchmark [13, 22] for which different research groups[5] have provided extensive benchmark-relevant data. In particular, for the first rising bubble test case, we will consider the data provided by group 1 of [22] as reference.

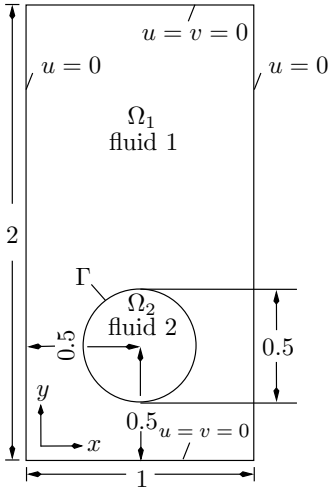

Figure 4: Configuration for the rising bubble test cases.

The rising bubble benchmark defines two test cases differing by their respective choice of the surface tension coefficient and the density and viscosity ratios of the fluids. We refer to Table 3 for a listing of the physical parameters of both test cases.

Test case	ρ_1	ρ_2	μ_1	μ_2	g	σ	Re	Eo	ρ_1/ρ_2	μ_1/μ_2
1	1000	100	10	1	0.98	24.5	49.5	9	10	10
2	1000	1	10	0.1	0.98	1.96	49.5	124.88	1000	100

Table 3: Physical parameters and dimensionless numbers defining the rising bubble test cases.

The problems are characterized by the dimensionless parameters density ratio ρ_1/ρ_2, viscosity ratio μ_1/μ_2, the Reynolds number $Re = \rho_1 \tilde{v} L/\mu_1$ and the Eötvös (or Bond) number $Eo = Bo = \Delta\rho g L^2/\sigma$, where we set the characteristic velocity to $\tilde{v} = \sqrt{g}$ and the characteristic length to $L = 2r$. Based on experimental findings, Clift et al. have published results (see Figure 2.5 in [7]) that render the bubble shape to be dependent on the combination of the Reynolds and Eötvös numbers. Albeit their results are for really three-dimensional bubbles, they can nonetheless be taken as a basis for qualitative comparisons. Based on their study, the combination shown for test case 1 is expected to produce an ellipsoidal shape, while due to the higher Eötvös number and thus smaller surface tension in test case 2, the bubble is expected to experience a more significant deformation. Therefore, in this case the bubble's shape is expected to be a blend between "skirted" and "dimpled ellipsoidal-cap" in Clift speak. In fact, our numerical bubble shapes presented in sections 5.2.1 and 5.2.2 are in good agreement with these experimental predictions.

[4] www.featflow.de

[5] TU Dortmund, Inst. of Applied Math: TP2D(FEM-Level Set),
EPFL Lausanne, Inst. of Analysis and Sci. Comp.: FreeLIFE (FEM-Level Set),
Uni. Magdeburg, Inst. of Analysis and Num. Math.: MooNMD (FEM-ALE).

For the quantification of the rising bubble dynamics, it is reasonable to compute a set of quantities such as the bubble's rise velocity V_b, center of mass Y_b and circularity $\not\epsilon$, being respectively defined as

$$\begin{aligned} A_b &= \int_{\Omega_2} 1 \, \mathrm{d}\boldsymbol{x}, \\ V_b &= \int_{\Omega_2} \boldsymbol{v}.y \, \mathrm{d}\boldsymbol{x}/A_b, \\ Y_b &= \int_{\Omega_2} \boldsymbol{x}.y \, \mathrm{d}\boldsymbol{x}/A_b, \\ \not\epsilon &= \frac{P_a}{P_b} = \frac{\text{perimeter of area-equivalent circle}}{\text{perimeter of bubble}} = \frac{2\pi\sqrt{A_b/\pi}}{P_b}, \end{aligned}$$

where A_b is both the area of the current bubble shape and the area of a circle with radius $r = \sqrt{A_b/\pi}$. For both rising bubble test cases we track the evolution of the bubble until the time $t_{\max} = 3$ and measure the temporal evolution of the above time dependent quantities with respect to the following relative error norms

$$\|e\|_1 = \frac{\sum_{t=1}^{N} |q_{t,\mathrm{ref}} - q_t|}{\sum_{t=1}^{N} |q_{t,\mathrm{ref}}|}, \qquad \|e\|_2 = \left(\frac{\sum_{t=1}^{N} |q_{t,\mathrm{ref}} - q_t|^2}{\sum_{t=1}^{N} |q_{t,\mathrm{ref}}|^2} \right)^{1/2}, \qquad \|e\|_\infty = \frac{\max_t |q_{t,\mathrm{ref}} - q_t|}{\max_t |q_{t,\mathrm{ref}}|},$$

where $\|e\|_1, \|e\|_2$ and $\|e\|_\infty$ respectively denote the l_1, l_2 and l_∞ relative error norms, $N = ((t_{\max} - t_1)/\Delta t) + 1$ is the number of time stepping sample points and q_t denotes the temporal evolution of quantity q. These relative error norms are eventually used to inspect the estimated order of convergence

$$\mathrm{EOC} = \frac{\log(\|e_{i-1}\|/\|e_i\|)}{\log(h_{i-1}/h_i)}$$

of the quantities V_b, Y_b and $\not\epsilon$. Note that the reference solution $q_{t,\mathrm{ref}}$ may possess a different time sampling concinnity than q_t. In such a situation interpolation is the means of choice to match the time steps.

5.2.1. Results for testcase 1

The relatively low Eötvös number of this setup implies non-negligible surface tension forces, compared to body forces. The surface tension forces can be thought of to act towards preserving the bubble shape and topology, and as aforementioned the combination of the Reynolds and Eötvös numbers of case 1 is expected to yield an ellipsoidal bubble geometry. Figure 5 illustrates, at different time steps, the shapes of our rising bubble alongside those computed with a [6]Q_2P_1 finite element discretization. The temporal development of the initially circular bubble is characterized in the early time stages $0 \leq t \leq 1.5$ by an horizontal stretching and dimple development. However, the shapes of the subsequent time steps disclose the clear endeavor to develop an ellipsoidal shape being in good conformity with experimental predictions. At all time instances our bubble shapes are in very good agreement with the results obtained with standard Q_2P_1 FE. Moreover, at final time $t_{\max}$, our approximated bubble geometry is shown to have a remarkable geometrical congruency with that of the reference solution (TP2D), having been superimposed over our data. Mesh convergence of our results is demonstrated in Figure 6, where the bubble shapes associated to different mesh family indices h are shown to match each other with respect to an acceptable tolerance. The diffuse interface method, however, introduces a diffuse interface width ξ which can be varied as well. It is

[6]Velocity: Biquadratic, continuous; Pressure: Linear (value and two partial derivatives), discontinuous

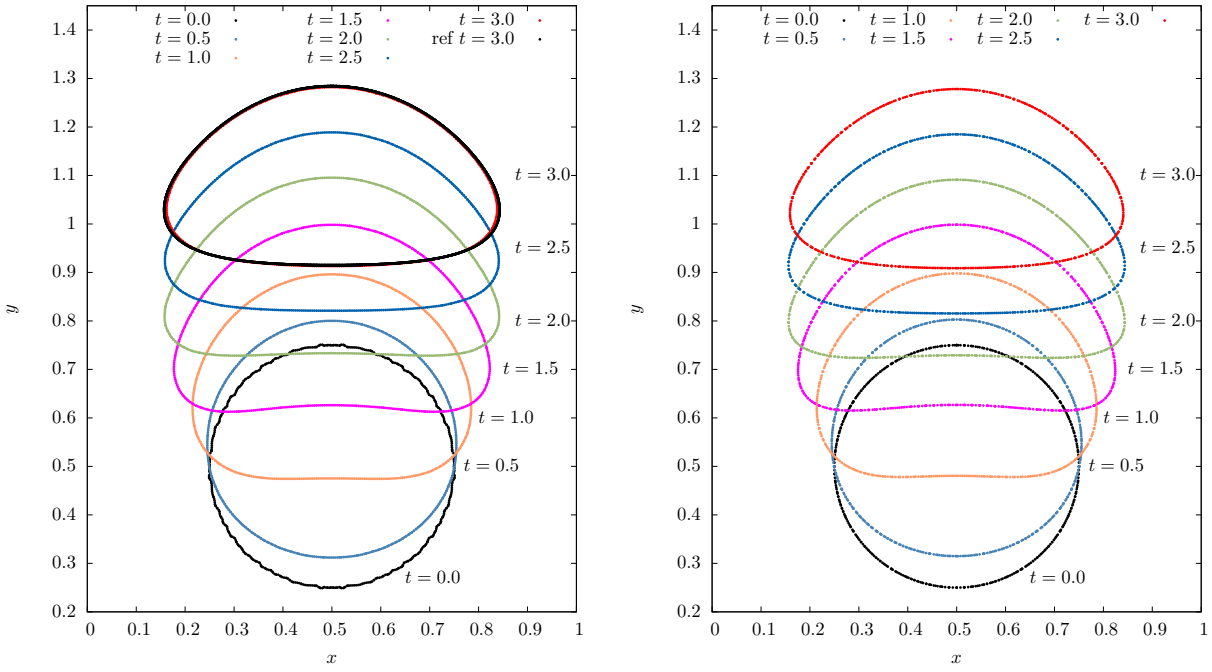

Figure 5: Shapes of the rising bubble at a set of time points. Left: Our results for $h = 2^{-6}$ and the TP2D reference shape at $t = t_{\max}$. Right: Level-set based sharp interface results computed with Q_2P_1 finite elements.

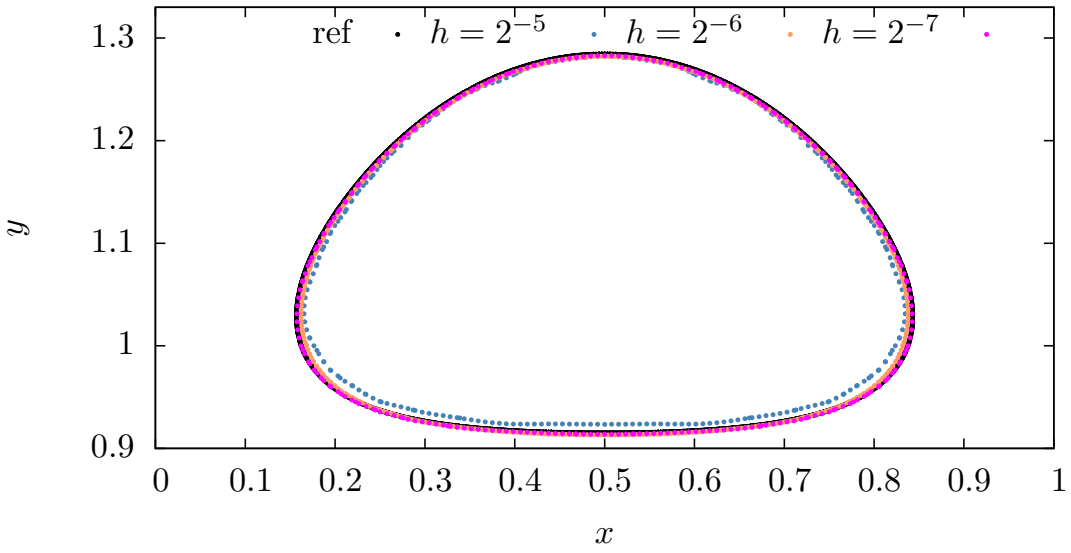

Figure 6: Shapes of the rising bubble at final time $t = 3$ for different h.

reasonable to set $\xi \propto h$ and, in fact, in all conducted computations for the first case of the rising bubble setup, the h, ξ and Δt settings of Table 4 together with mobility coefficient $D = 0.00004$ (cf. (17)) were used. The effect of modifying the diffuse interface width while keeping the mesh

h	ξ	Δt	$\not{\epsilon}_{\min}$	$t\vert_{\not{\epsilon}=\not{\epsilon}_{\min}}$	$V_{b,\max}$	$t\vert_{V_b=V_{b,\max}}$	$Y_b(t=3)$
2^{-4}	0.040	0.008	0.9425	2.1281	0.2384	1.2000	1.0665
2^{-5}	0.020	0.008	0.9151	1.9280	0.2423	0.9520	1.0778
2^{-6}	0.010	0.004	0.9044	1.9240	0.2422	0.9120	1.0792
2^{-7}	0.005	0.004	0.9013	1.9200	0.2420	0.9200	1.0794
ref			0.9013	1.9041	0.2417	0.9213	1.0813

Table 4: Minimum circularity and maximum rise velocity with corresponding incidence times and final position of the center of mass for test case 1.

refinement level fixed is demonstrated in Figure 7. For three consecutive diffuse interface widths

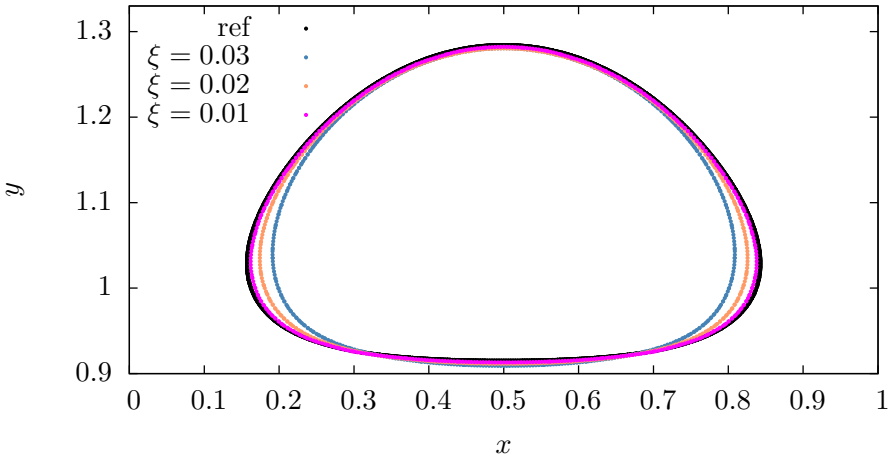

Figure 7: Shapes of the rising bubble at final time $t = 3$ for $h = 2^{-6}, \Delta t = 0.004$ and different diffuse interface widths.

$\xi = 0.03, 0.02, 0.01$ on the exemplary chosen mesh refinement level 6, the results are shown to converge to the reference as ξ decreases. The choice of ξ needs to respect the size of h as without a "reasonable" amount of elements across the diffuse interface width, the numerics will fail to produce rational results due to undersampling effects.

Devoting our attention back to the previously defined benchmark quantities V_b, Y_b and $\not{\epsilon}$, we present in Figure 9 our results for their temporal evolution. For decreased h the profiles of all quantities converge to the reference. On the highest displayed refinement level, the congruency of our profiles with the reference is remarkable. Extrema of these profiles, such as minimum circularity $\not{\epsilon}_{\min}$, maximum rise velocity $V_{b,\max}$ and final center of mass $Y_b(t = 3)$ together with their incidence times are tabulated in Table 4 for different mesh refinement levels. On levels 6 and 7, our approximations of $V_{b,\max}, Y_b(t = 3)$ and $\not{\epsilon}_{\min}$ respectively exhibit 3 and 2 matching decimal digits, when compared to each other. Besides, the quantities are shown to converge to the reference values. The relative error norms and the respective convergence orders of the quantities center of mass, rise velocity and circularity are illustrated in Table 5. For the quantities center of mass and rise velocity, the convergence orders of the l_1 and l_2 errors are around 1, while we approach quadratic convergence in case of circularity. For all quantities, the convergence order of the l_∞ error is as a matter of principle

q	h	ξ	$\|e\|_1$	EOC_1	$\|e\|_2$	EOC_2	$\|e\|_\infty$	EOC_∞
Y_b	2^{-4}	0.040	0.0171		0.0183		0.0217	
	2^{-5}	0.020	0.0053	1.7049	0.0057	1.6818	0.0078	1.4755
	2^{-6}	0.010	0.0019	1.4633	0.0020	1.5127	0.0026	1.5947
	2^{-7}	0.005	0.0013	0.5312	0.0013	0.5706	0.0014	0.8730
V_b	2^{-4}	0.040	0.0516		0.0559		0.0775	
	2^{-5}	0.020	0.0206	1.3263	0.0219	1.3518	0.0321	1.2714
	2^{-6}	0.010	0.0051	2.0064	0.0059	1.8934	0.0121	1.4112
	2^{-7}	0.005	0.0023	1.1755	0.0028	1.0575	0.0061	0.9790
ϕ	2^{-4}	0.040	0.0267		0.0317		0.0431	
	2^{-5}	0.020	0.0095	1.4927	0.0111	1.5095	0.0152	1.5051
	2^{-6}	0.010	0.0023	2.0446	0.0027	2.0443	0.0040	1.9111
	2^{-7}	0.005	0.0005	2.1778	0.0007	2.0334	0.0013	1.6871

Table 5: Relative error norms and estimated orders of convergence of the benchmark quantities for test case 1. Errors have been computed w.r.t. the sharp interface reference solution.

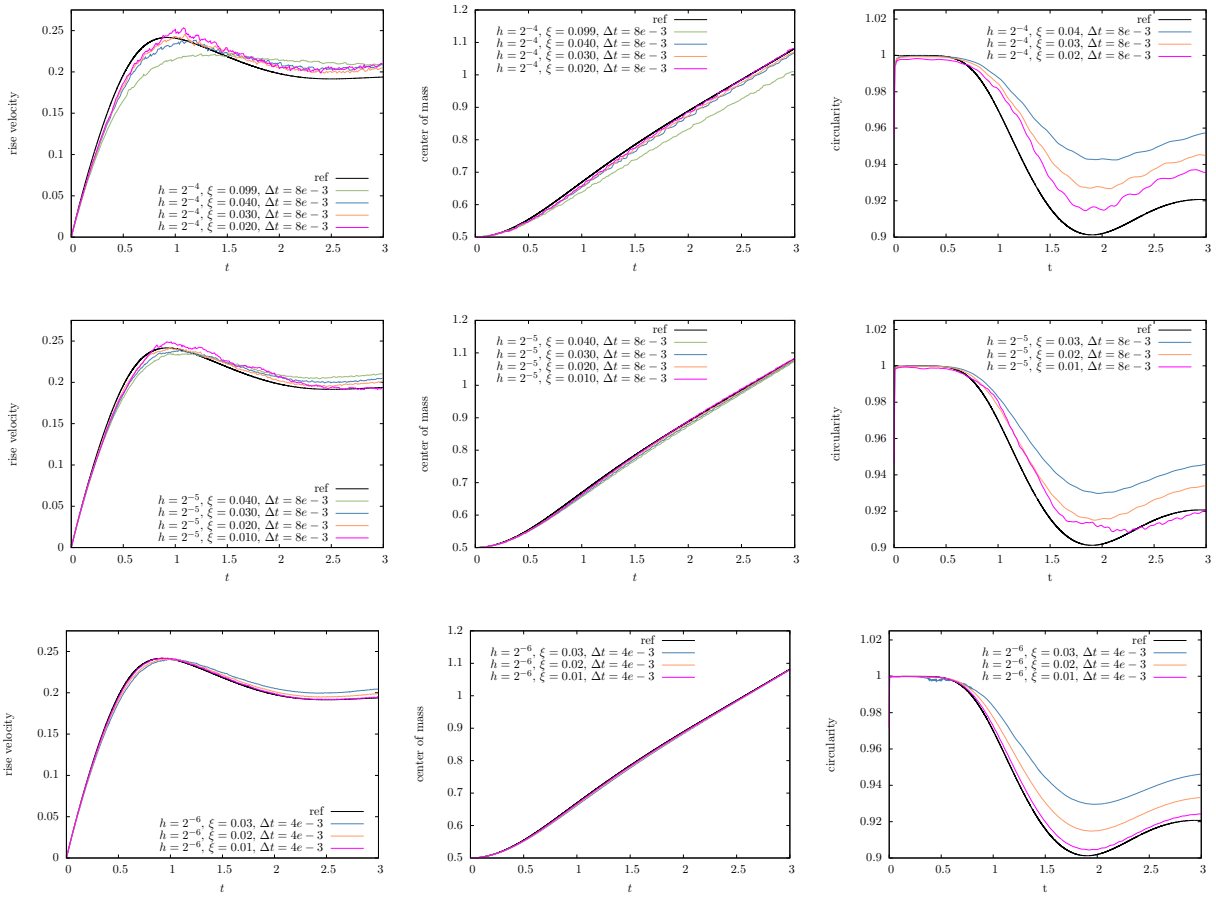

Figure 8: Rising bubble test case 1: Influence of the diffuse interface width ξ on the rise velocity and center of mass profiles for $h = 2^{-4}$, 2^{-5}, 2^{-6}.

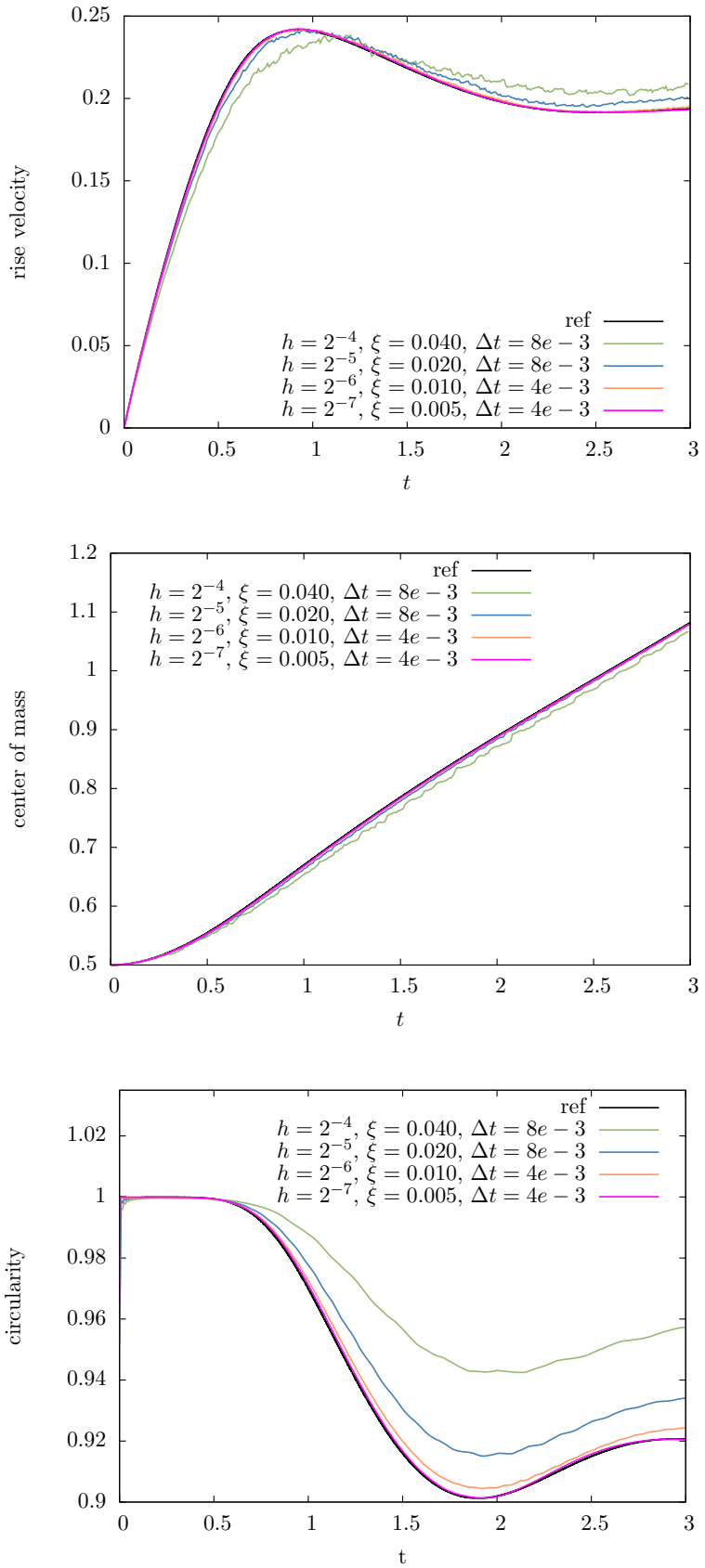

Figure 9: Rising bubble test case 1: Rise velocity, center of mass and circularity profiles (mobility = 0.00004).

slightly lower than its counterparts. Note that the errors depicted in Table 5 are computed with respect to the sharp interface reference solution $q_{t,\text{ref}}$ published in [22]. Their computation of the l_1, l_2 and l_∞ errors consider their own solution on the finest grid to be the exact solution.

For the sake of a fair comparison with diffuse interface models, we therefore extend our analysis to the same mode, that is, taking our finest grid solution as the reference. Doing so, clearly improves the convergence orders as illustrated in Table 6. Again, the convergence orders of the l_∞ errors are by trend smaller than those of the l_1 and l_2 errors. The latter mentioned are around 2 for all quantities. Finally, in order to inspect the influence of the diffuse interface width on the accuracy

q	h	ξ	$\|e\|_1$	EOC_1	$\|e\|_2$	EOC_2	$\|e\|_\infty$	EOC_∞
Y_b	2^{-4}	0.040	0.0158		0.0170		0.0206	
	2^{-5}	0.020	0.0039	2.0024	0.0045	1.9263	0.0068	1.6026
	2^{-6}	0.010	0.0007	2.5718	0.0008	2.5136	0.0015	2.2132
V_b	2^{-4}	0.040	0.0505		0.0549		0.0748	
	2^{-5}	0.020	0.0193	1.3883	0.0209	1.3969	0.0323	1.2100
	2^{-6}	0.010	0.0037	2.3780	0.0042	2.3116	0.0076	2.0974
ϕ	2^{-4}	0.040	0.0261		0.0312		0.0428	
	2^{-5}	0.020	0.0090	1.5363	0.0107	1.5463	0.0198	1.1128
	2^{-6}	0.010	0.0018	2.3055	0.0022	2.2597	0.0063	1.6609

Table 6: Relative error norms and estimated convergence orders of the benchmark quantities for test case 1 assuming the finest grid solution as exact solution.

of the results, we have extended the analysis of the temporal development of the quantities to the situation where for each mesh refinement level, the diffuse interface width is varied. The results, depicted in Figure 8, disclose as expected an improvement of the results in terms of accuracy as the mesh refinement level and diffuse interface width approach a more favorable relation.

5.2.2. Results for testcase 2

Compared to the first rising bubble setup, the second one is characterized by significantly higher density and viscosity ratios and a higher Eötvös number. This implies both a tremendous different amount of body forces acting on either side of the fluid-fluid interface and rather negligible surface tension forces, compared to body forces. As a consequence, the bubble is subject to significant deformations giving rise to the development of thin filaments at its lower left and right corners. As the bubble keeps rising due to buoyancy forces, these filaments experience elongation and develop an ever thinner getting region implying a break off in the limit. This problem involves large force gradients across the diffuse interface and is thus much harder to solve than the first rising bubble test case. As a matter of fact, the results produced by different numerical techniques in [22] are in no good agreement, particularly with regard to the second half of the computational time span. Moreover, it is not even clear whether break off is to occur. After all, according to experimental tests with three dimensional bubbles the shape is expected to be a blend between "skirted" and "dimpled ellipsoidal-cap". By analogy with the first test case, we analyze the benchmark quantities and the bubble shapes, however using now the simulation parameters of Table 7. We refer to Figure 10 for a depiction of the temporal evolution of the bubble shape at mesh refinement level 7. The initial circular shape is shown to gradually develop two filaments on its sides as it experiences an upward pushing force. The lower right image illustrates the final bubble shapes of three different "reference" groups. While the filaments computed with the diffuse interface method show a smooth and symmetric shape, those of the reference groups show less regularity. In fact, one of them even

h	ξ	Δt	D
2^{-4}	0.040	0.008	0.000040
2^{-5}	0.020	0.004	0.000040
2^{-6}	0.010	0.002	0.000020
2^{-7}	0.005	0.001	0.000005

Table 7: Numerical parameters for the rising bubble test case 2.

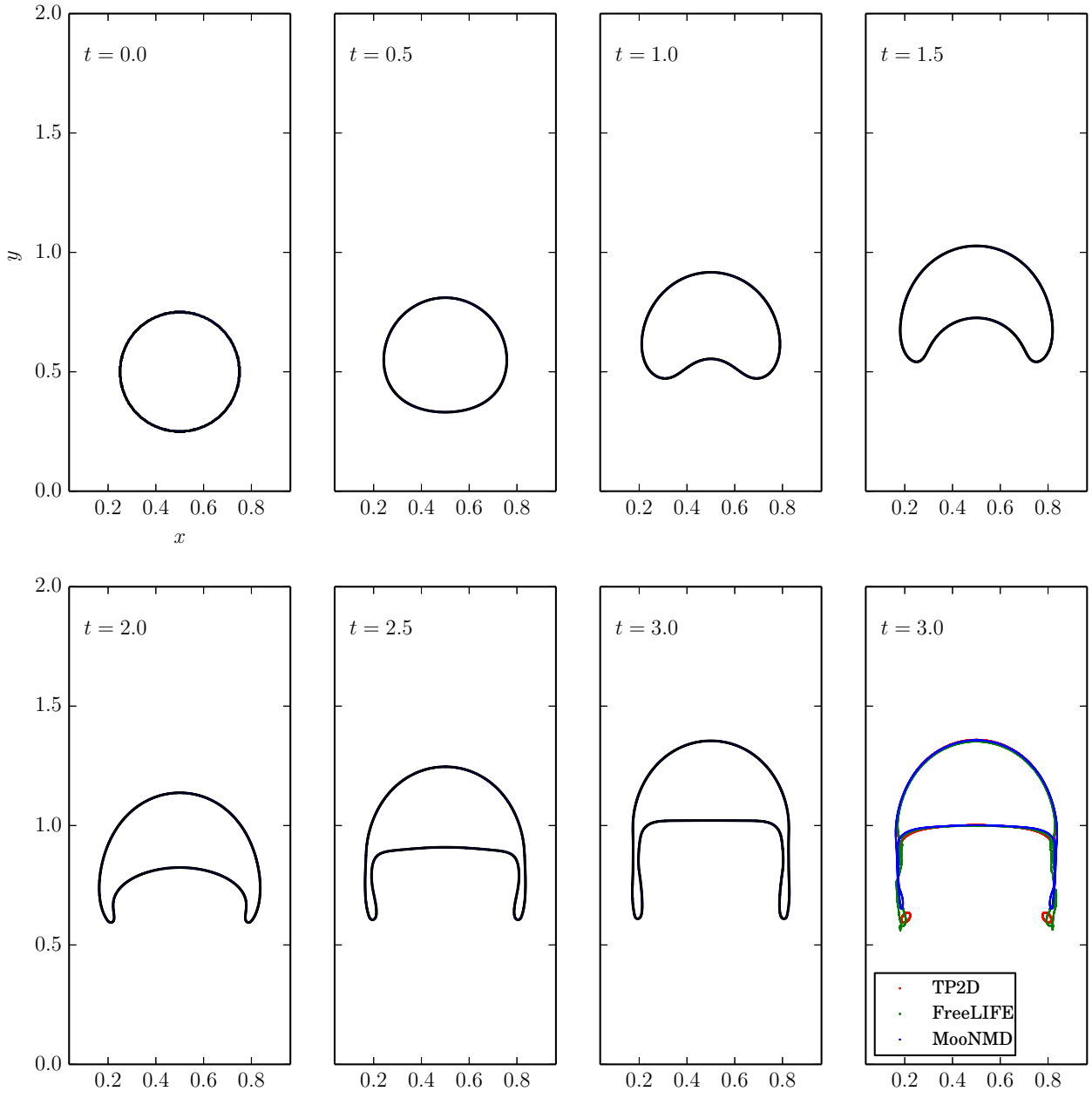

Figure 10: Shapes of the rising bubble at a set of time points for $h = 2^{-7}$.

exhibits break off of the filaments and the formation of two satellite drops. In contrast to this, our results never showed break off at any tested mesh refinement level as demonstrated in Figure 11.

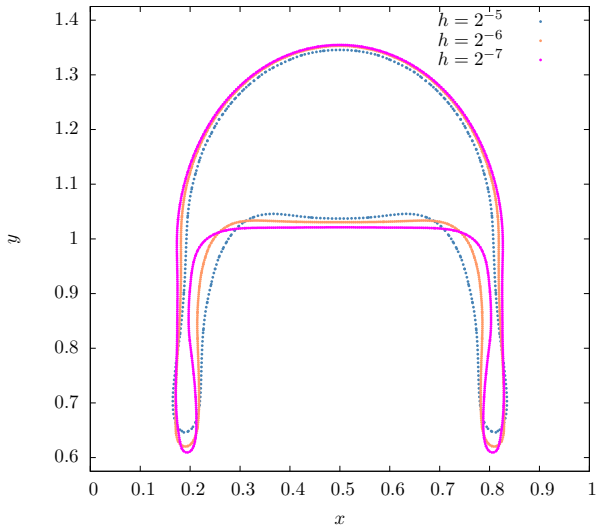

Figure 11: Shapes of the rising bubble at final time $t = 3$ for different h.

It is, however, obvious that at higher mesh refinement levels the filaments tend to become thinner in their upper part which also imply narrower diffuse interfaces. Therefore, one may bring forward the argument that for $h \to 0$ and $\varepsilon \to 0$ with $\varepsilon \propto h$, the left and right boundaries of a filament at its narrowest region may come arbitrary close to each other, including the possibility to merge, that renders a break off inevitable.

The temporal evolution of the quantities V_b, Y_b and $\not\in$ for different mesh refinement levels is depicted in Figure 12. In contrast to the reference rise velocity profile of the first rising bubble test case, we see two extrema roughly around times $t = 0.72$ and $t = 2.08$. The emergence of the second crest temporarily coincides with the development, elongation and the eventual shedding of the filaments. This in turn is believed to yield a more streamlined geometry which reduces the drag force and allows for a higher rise velocity. For our filaments are shown to never break off and to have an average thickness larger than those of the reference groups, the above described effect is expected to be less pronounced than in reference results. This is in fact reflected by the clear deviation of the phase field based rise velocity profiles around the second half of the simulation time span. Our profiles for the center of mass exhibit convergence and are in good correlation with the reference roughly until time $t = 2$. Following the arguments presented above, the missing or the rather smaller extra speed impulse results in a slightly shorter traveled distance. The sudden jump in the circularity profile of the reference happens around time $t = 2.4$ which happens to be nothing else but the break off moment. Therefore, it is reasonable to set this time instance as the upper bound when it comes to comparisons of the circularity profiles. Our approximations of the latter are shown to be converged and, except for a small deviation in the time interval $[1.6, 2.4]$, to be in good consensus with the reference.

Again, for different mesh refinement levels, extrema of the benchmark quantities together with their incidence times are listed in Table 8. Due to the lack of an accepted reference, we have presented the "quasi"-reference results at our disposal to whom our results are compared. Bearing in mind that by virtue of the difficulties to solve this problem even the sharp interface-based quasi-reference results are in no satisfactory agreement, it would be presumptuous to expect the diffuse interface results to converge to one of these. Nevertheless, our approximations reflect the quasi-reference

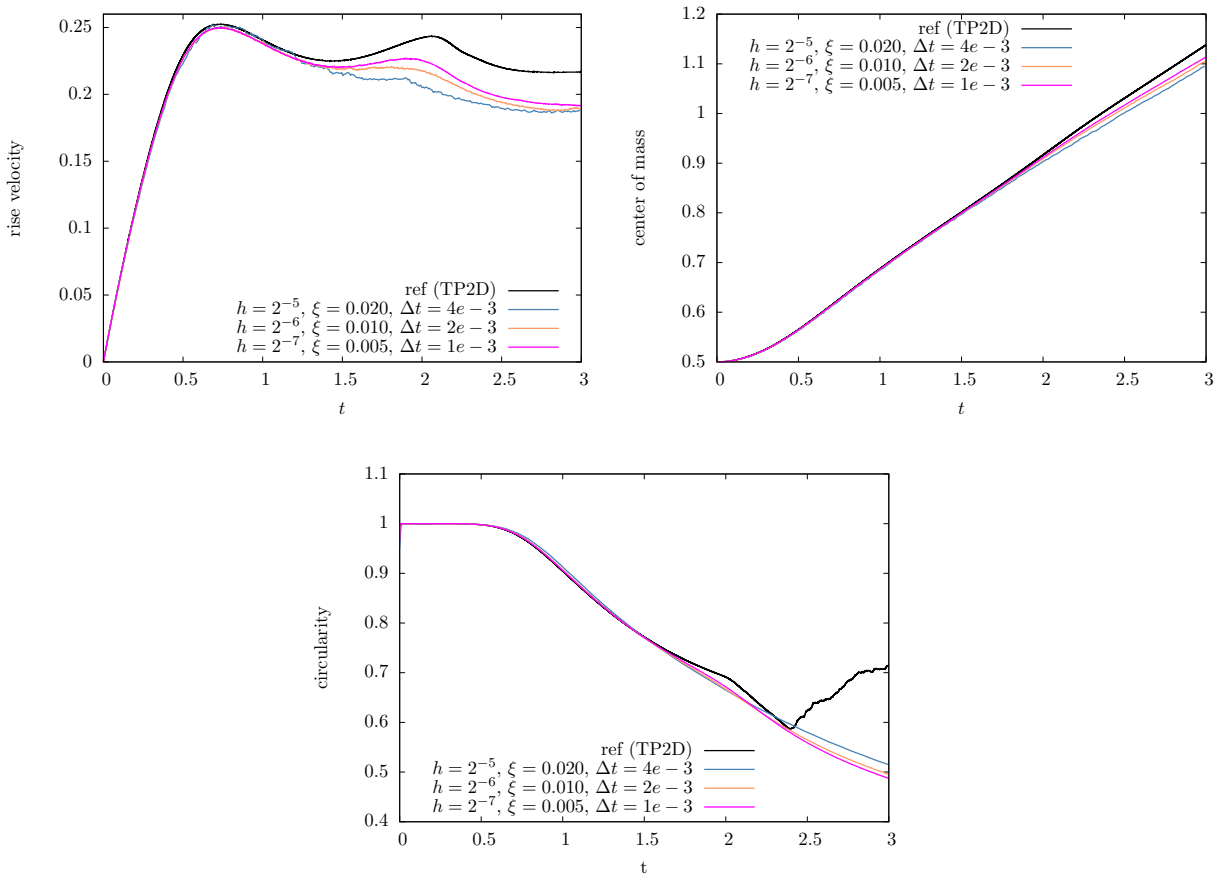

Figure 12: Rising bubble test case 2: Rise velocity, center of mass and circularity profiles.

h	ξ	Δt	$\phi_{\min}$	$t\|_{\phi=\phi_{\min}}$	$V_{b,\max}$	$t\|_{V_b=V_{b,\max}}$	$Y_b(t=3)$
2^{-5}	0.020	0.004	0.5147	3	0.2520	0.6800	1.0952
2^{-6}	0.010	0.002	0.4952	3	0.2505	0.7680	1.1058
2^{-7}	0.005	0.001	0.4872	3	0.2498	0.7450	1.1137
TP2D			0.5869	2.4004	0.2524	0.7332	1.1380
FreeLIFE			0.4647	3	0.2514	0.7581	1.1249
MooNMD			0.5144	3	0.2502	0.7317	1.1376

Table 8: Minimum circularity and maximum rise velocity with corresponding incidence times and final position of the center of mass for test case 2.

results and $\phi_{\min}$ and $Y_b(t=3)$ seem to converge to the figures of FreeLIFE.

Continuing the quantitative analysis, we present in Table 9 the relative error norms and the respective estimated convergence orders of the quantities center of mass, rise velocity and circularity. It's noteworthy to mention that for the computation of the l_1, l_2 and l_∞ errors and their convergence

q	h	ξ	$\|e\|_1$	EOC_1	$\|e\|_2$	EOC_2	$\|e\|_\infty$	EOC_∞
Y_b	2^{-5}	0.020	0.0185		0.0208		0.0263	
	2^{-6}	0.010	0.0067	1.4620	0.0073	1.5072	0.0095	1.4755
	2^{-7}	0.005	0.0023	1.5358	0.0025	1.5600	0.0031	1.5947
V_b	2^{-5}	0.020	0.0458		0.0520		0.0775	
	2^{-6}	0.010	0.0185	1.3060	0.0201	1.3710	0.0321	1.2714
	2^{-7}	0.005	0.0063	1.5620	0.0068	1.5643	0.0121	1.4112
ϕ	2^{-5}	0.020	0.0208		0.0277		0.0431	
	2^{-6}	0.010	0.0078	1.4147	0.0102	1.4478	0.0152	1.5051
	2^{-7}	0.005	0.0022	1.8389	0.0027	1.8880	0.0040	1.9111

Table 9: Relative error norms and estimated orders of convergence of the benchmark quantities for test case 2. Errors have been computed w.r.t. the TP2D sharp interface reference solution.

orders the considered time interval has been confined to $[0, 2]$, since for later times the reference solutions do not agree either. For all quantities the relative errors in all norms are shown to converge to 0 with a linear order of convergence. By analogy with the proceeding in the first rising bubble test case, we extend the study of the relative error convergence orders to the case where our solution on the finest mesh is taken as the exact value. This corresponds to the approach used in [22]. Measuring the errors with respect to this alternative reference, yields a considerable improvement and in fact shifts the convergence orders towards the quadratic region. (See Table 10.)

q	h	ξ	$\|e\|_1$	EOC_1	$\|e\|_2$	EOC_2	$\|e\|_\infty$	EOC_∞
Y_b	2^{-4}	0.040	0.0158		0.0170		0.0206	
	2^{-5}	0.020	0.0039	2.0024	0.0045	1.9263	0.0068	1.6026
	2^{-6}	0.010	0.0007	2.5718	0.0008	2.5136	0.0015	2.2132
V_b	2^{-4}	0.040	0.0505		0.0549		0.0748	
	2^{-5}	0.020	0.0193	1.3883	0.0209	1.3969	0.0323	1.2100
	2^{-6}	0.010	0.0037	2.3780	0.0042	2.3116	0.0076	2.0974
ϕ	2^{-4}	0.040	0.0261		0.0312		0.0428	
	2^{-5}	0.020	0.0090	1.5363	0.0107	1.5463	0.0198	1.1128
	2^{-6}	0.010	0.0018	2.3055	0.0022	2.2597	0.0063	1.6609

Table 10: Relative error norms and estimated convergence orders of the benchmark quantities for test case 2 assuming the finest grid solution as exact solution.

5.3. Rayleigh-Taylor instability

The Rayleigh-Taylor instability is a two-phase instability which occurs whenever two fluids of different density are accelerated against each other. Any perturbation along the interface between a heavy fluid (F_H) on top of a lighter fluid (F_L), both subject to a gravitational field, gives rise to the phenomenon of Rayleigh-Taylor instability. The initial perturbations progress from an initial linear growth phase into a non-linear one, eventually developing "mushroom head" like structures moving upwards and thinning "spikes" falling downwards. Assuming negligible viscosity and surface tension, the instability is characterized by the density disparity, measured with the Atwood number

$\mathcal{A} = (\rho_H - \rho_L)/(\rho_H + \rho_L)$. For the validation of our results, we will consider the works of Tryggvason [36] and Guermond et al. [15] as reference. The former investigated the initial growth and long-time evolution of the instability for incompressible and inviscid flows with zero surface tension at $\mathcal{A} = 0.5$. Guermond et al., on the other hand, studied this instability problem at the same Atwood number, however, taking viscous effects additionally into account.

The setup of the problem is described by a rectangular computational domain $[0, d] \times [0, 4d]$, where an initial wavy interface segregates a heavier fluid in the upper domain part from a lighter fluid on the lower part. The initial interface is described by the function

$$y(x) = 2d + 0.1d\cos(2\pi x/d)$$

representing a planar interface superimposed by a perturbation of wave number $k = 1$ and amplitude $0.1d$. Note that setting the surface tension coefficient σ to 0, effectively downgrades the Cahn-Hilliard equation (25) to a pure transport equation well known from the level-set context. This, in turn, implies to pass on both the physical benefits inherent to phase field models and to the automatic recreation of the smooth transition of the phase field in the interface region. In order to circumvent these issues, we chose to set the surface tension coefficient to the small, yet non-zero value 0.01. As for the remaining simulation parameters we set $d = 1, \rho_H = 3, \rho_L = 1, \mu_H = \mu_L = 0.0031316$ and $g = 9.80665$, giving rise to $\mathcal{A} = 0.5$ and $Re = \rho_H d^{3/2} g^{1/2}/\mu_H = 3000$. At the top and bottom boundaries we use the no-slip boundary condition, whereas the free slip boundary condition is imposed on the vertical walls. Figure 13 depicts our results for the temporal evolution of the interface computed in the time interval $[0, 1.5]$ with $\Delta t = 0.001, h = 2^{-7}, \varepsilon = 0.005$ and $D = 0.00004$.

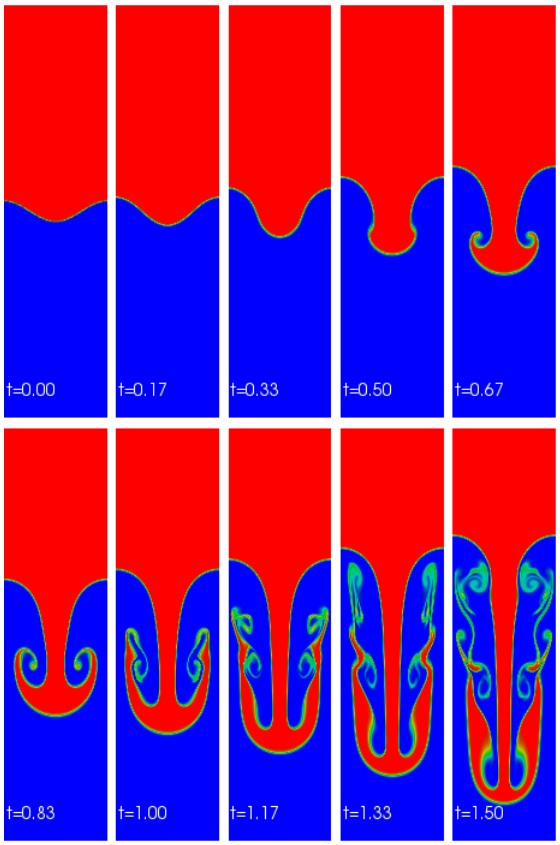

Figure 13: The evolution of a single wavelength initial condition in the Rayleigh-Taylor instability simulation.

As anticipated, the heavier fluid on top starts to fall through the lighter fluid and gradually develops spikes which are subject to strong deformations. When it comes to the comparison of the vortex structure with the "inviscid" results of Tryggvason and the "viscous" results of Guermond et al., our viscous solution exhibits a satisfactory agreement with both, especially with the latter mentioned. Note that the data provided by the above references are computed with respect to individual scalings of the involved PDE variables in order to obtain nondimensional variables. Therefore, comparisons require the time scales of the respective simulations to be mapped to each other. Since, in contrast to the reference results, we did not perform any rescaling, our time t is mapped to Tryggvason's time $\tilde{t}$ via the relation $t = \sqrt{d/(\mathcal{A}\, g)}\, \tilde{t}$.

We continue the validation of our results with a quantitative analysis and conduct a comparison of the tip of the rising and falling fluids with the inviscid and viscous results provided by Tryggvason and Guermond et al., respectively. The results, depicted in Figure 14, correspond well with both references whose data have individually been translated along the y-axis to facilitate comparisons.

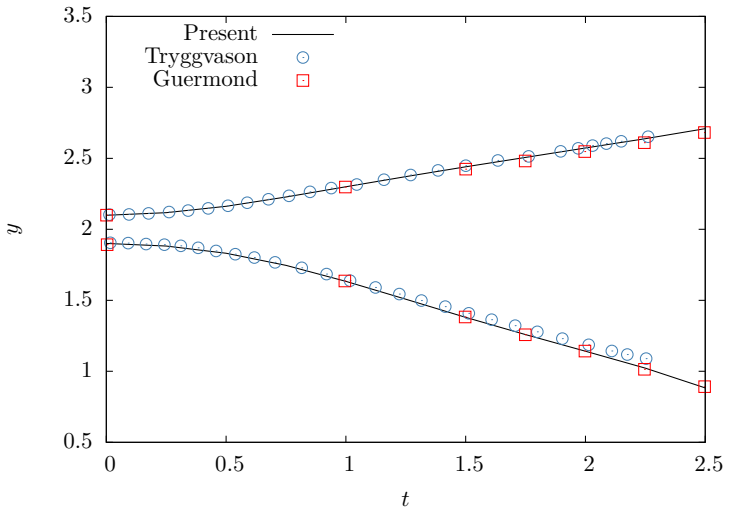

Figure 14: The y-coordinate of the tip of the rising and falling fluid versus time.

The upper curve referring to the tip of the rising fluid shows a better correlation with the data provided by Tryggvason while our curve for the falling fluid seems to perfectly match the results of Guermond. The analysis is finally concluded with the examination of the interface structure at a randomly selected fixed time $t = 0.79031$ for three consecutive meshes of global mesh size $h = 2^{-5}$, 2^{-6}, 2^{-7} pointing to a refinement level index. As shown in Figure 15, the main difference between the figures is in the level of detail of the vortices. While there is only little roll-up in the coarse grid case, the vortices on the finest grid exhibit a tightly wound spiral. Besides, the y-coordinate of the tip of the rising and falling fluid slightly differ from one level to the other and are thus regarded as weakly resolution dependent. Apart from that no significant differences can be observed.

6. Summary and conclusions

In this work, we have presented our numerical results of the application of Galerkin-based Isogeometric Analysis to incompressible Navier–Stokes–Cahn–Hilliard equations in velocity–pressure–phase field–chemical potential formulation. In this formulation the fourth order Cahn–Hilliard equation is split into two second order equations, effectively introducing the chemical potential η as

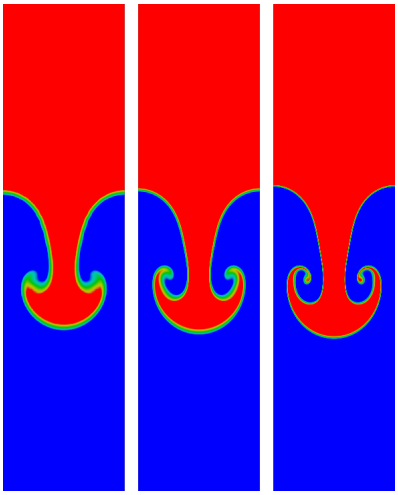

Figure 15: Rayleigh-Taylor instability simulation at time $t = 0.79031$ for three consecutive mesh refinement levels.

a new variable. The reason we have preferred the splitted version over the original one is twofold: firstly depending on the way the surface tension force is modeled on top of the Navier–Stokes equations, the computation of the chemical potential may become a necessity and secondly we avoid complications with nonlinear boundary conditions arising from the discretization of the equation in its primal form. Nevertheless, Isogeometric Analysis easily allows to setup discrete approximation spaces with high continuity as for instance demonstrated in [21] for the case of one-phase flow.

The velocity and pressure functions were approximated with LBB stable non-uniform rational B-spline spaces which can be regarded as smooth generalizations of Taylor–Hood pairs of finite element space. The governing equations were discretized in time fully implicitly ($\theta >= 0.5$) with the one-step θ-scheme and finally solved blockwise, that is, solving the phase field system with the current velocity field and eventually using the phase field variables to solve the two-phase flow equations.

The static bubble, rising bubble and the Rayleigh-Taylor instability flow scenarios were considered in two dimensions as model problems in order to investigate the numerical traits and behavior of the Isogeometric discretization.

Starting off with the static bubble scenario, we have shown that the approximated velocity field is perturbed by spurious currents of order 10^{-4} downto 10^{-5} and the pressure jump across the interface behaves according to theoretical predictions. Moreover, the velocity and pressure fields were shown to be very well comparable with reference sharp interface model results, as for instance [37].

In addition to the static bubble, we extended the application of Galerkin-based Isogeometric Analysis to the prominent rising bubble benchmarks, as proposed in [13, 22], and analyzed the approximated benchmark quantities such as the bubble's rise velocity, center of mass and circularity with respect to accuracy and convergence. For the first rising bubble benchmark characterized by a relatively moderate density ratio, our results were shown to integrate very well with the reference data. In fact, with increased mesh refining the time profiles of the mentioned quantities exposed rapid convergence to the reference and were visually indistinguishable from it on the highest mesh refinement level. We extended the analysis to the inspection of the effect of different diffuse interface widths on a fixed mesh refinement level. The study, expectedly, rendered the accuracy to be sensitive to the ratio of the diffuse interface width and the mesh refinement level and to profit from reasonable settings. Moreover, the analysis was extended to inspect the convergence orders of l_1, l_2 and l_∞

relative errors of additional benchmark quantities, whereby the errors were computed w.r.t to both the reference results and our own results obtained on the mesh with the highest resolution. Referring to these two cases, the errors showed linear and quadratic convergence, respectively.

The second and more challenging rising bubble benchmark involves a large density ratio and a low surface tension which in turn implies large gradients of quantities such as e.g. pressure and severe shape deformations up to topological changes in the limit case. We point out that due to the difficulties to solve this problem, since at least the second half of the simulation time interval, the available references are in no good correspondence with each other. So are our approximations with regard to these references and it is in fact not even clear weather the elongated bubble filaments are to break off or not. The same analysis as in the first rising bubble test case was performed for the second test case as well with very similar results.

In order to demonstrate the robustness of the method, we included the Rayleigh-Taylor instability problem having become a popular test case for numerical methods intended to study multiphase or multimaterial problems. Using the setup and reference results of Tryggvason [36] and Guermond et al. [15], we analyzed the evolution of a single wavelength interface perturbation. Qualitative comparisons of the interface shapes and quantitative analysis of the positions of the tip of the rising and falling fluid rendered our approximations to be in good correlation with the above references. Moreover, we showed our results to be mesh converged, since the produced data associated to different mesh resolutions are well comparable except for the high resolution features such as the roll-up spirals emerging at higher mesh refinement levels.

The efficient solution of the arising linear equation systems with iterative techniques such as, for instance, multigrid were out of the scope of this study and will therefore be addressed in a forthcoming publication.

Isogeometric Analysis proved for us to be a robust and powerful technology showcasing well applicability to multiphase flow problems. Bearing in mind that, in contrast to the simple geometries involved in the considered benchmarks, simulations of real world multiphase flow problems need to cope with very complex geometries, the combination of Isogeometric Analysis and phase field based multiphase flow models may be a very good alternative to sharp interface models involving straight line segment approximation of curved domain boundaries. This is motivated by the fact that computations on exact geometries avoid any modification of the original computational domain and proved in a row of different contexts to be beneficial accuracy wise [8]. Moreover, Isogeometric Analysis is best suited for the numerical approximation of the fourth order Cahn–Hilliard equations in their primal formulation requiring a discrete approximation space with $\mathcal{C}^1$ regularity. The Cahn–Hilliard phase field model is equipped with the benefits to minimize interface energy, to be mass conservative and to avoid typical hassles involved with level-set methods such as for instance redistancing.

References

[1] H. Abels, H. Garcke, and G. Grün. Thermodynamically consistent, frame indifferent diffuse interface models for incompressible two-phase flows with different densities. *Mathematical Models and Methods in Applied Sciences*, 22(03):1150013, 2012.

[2] S. Aland and A. Voigt. Benchmark computations of diffuse interface models for two-dimensional bubble dynamics. *International Journal for Numerical Methods in Fluids*, 69(3):747–761, 2012.

[3] V. E. Badalassi, H. D. Ceniceros, and S. Banerjee. Computation of multiphase systems with phase field models. *Journal of Computational Physics*, 190(2):371 – 397, 2003.

[4] D. Bhaga and M. E. Weber. Bubbles in viscous liquids: shapes, wakes and velocities. *Journal of Fluid Mechanics*, 105:61–85, 4 1981.

[5] F. Boyer. A theoretical and numerical model for the study of incompressible mixture flows. *Computers and Fluids*, 31(1):41–68, 2002.

[6] L. Chen, S. V. Garimella, J. A. Reizes, and E. Leonardi. The development of a bubble rising in a viscous liquid. *Journal of Fluid Mechanics*, 387:61–96, 1999.

[7] R. Clift, J. R. Grace, and M. E. Weber. *Bubbles, Drops, and Particles*. Academic Press, 1978.

[8] J. A. Cottrell, T. J. R. Hughes, and Y. Bazilevs. *Isogeometric Analysis: Toward Integration of CAD and FEA*. Wiley Publishing, 1st edition, 2009.

[9] A. Debussche and L. Dettori. On the cahn-hilliard equation with a logarithmic free energy. *Nonlinear Analysis*, 24(10):1491–1514, 1995.

[10] H. Ding, P. D. M. Spelt, and C. Shu. Diffuse interface model for incompressible two-phase flows with large density ratios. *Journal of Computational Physics*, 226(2):2078 – 2095, 2007.

[11] N. Dubash and I. Frigaard. Conditions for static bubbles in viscoplastic fluids. *Physics of Fluids*, 16(12):4319–4330, 2004.

[12] L. F. R. Espath, A. F. Sarmiento, P. Vignal, B. O. N. Varga, A. M. A. Cortes, L. Dalcin, and V. M. Calo. Energy exchange analysis in droplet dynamics via the navier–stokes–cahn–hilliard model. *Journal of Fluid Mechanics*, 797:389–430, 6 2016.

[13] `http://www.featflow.de/en/benchmarks/cfdbenchmarking/bubble.html` [Online; accessed 08-Feb-2016].

[14] S. Ganesan, G. Matthies, and L. Tobiska. On spurious velocities in incompressible flow problems with interfaces. *Computer Methods in Applied Mechanics and Engineering*, 196(7):1193–1202, 2007.

[15] J.-L. Guermond and L. Quartapelle. A projection fem for variable density incompressible flows. *Journal of Computational Physics*, 165(1):167 – 188, 2000.

[16] Z. Guo, P. Lin, and J. S. Lowengrub. A numerical method for the quasi-incompressible cahn–hilliard–navier–stokes equations for variable density flows with a discrete energy law. *Journal of Computational Physics*, 276:486 – 507, 2014.

[17] M. E. Gurtin, D. Polignone, and J. Vinals. Two-phase binary fluids and immiscible fluids described by an order parameter. *Mathematical Models and Methods in Applied Sciences*, 6(6):815–831, 1996.

[18] H. Gómez, V. M. Calo, Y. Bazilevs, and T. J. R. Hughes. Isogeometric Analysis of the Cahn-Hilliard phase-field model. *Computer Methods in Applied Mechanics and Engineering*, 197(49-50):4333–4352, 2008.

[19] C. W. Hirt and B. D. Nichols. Volume of fluid (vof) method for the dynamics of free boundaries. *Journal of Computational Physics*, 39(1):201 – 225, 1981.

[20] P. C. Hohenberg and B. I. Halperin. Theory of dynamic critical phenomena. *Reviews of Modern Physics*, 49:435–479, Jul 1977.

[21] B. S. Hosseini, M. Möller, and S. Turek. Isogeometric Analysis of the Navier-Stokes equations with Taylor-Hood B-spline elements. *Applied Mathematics and Computation*, 267:264–281, 2015.

[22] S. Hysing, S. Turek, D. Kuzmin, N. Parolini, E. Burman, S. Ganesan, and L. Tobiska. Quantitative benchmark computations of two-dimensional bubble dynamics. *International Journal for Numerical Methods in Fluids*, 60(11):1259–1288, 2009.

[23] J. Giesselmann and T. Pryer. Energy consistent discontinuous galerkin methods for a quasi-incompressible diffuse two phase flow model. *ESAIM: Mathematical Modeling and Numerical Analysis*, 49(1):275–301, 2015.

[24] D. Jacqmin. Calculation of two-phase navier–stokes flows using phase-field modeling. *Journal of Computational Physics*, 155(1):96 – 127, 1999.

[25] C. Josserand and S. T. Thoroddsen. Drop impact on a solid surface. *Annual Review of Fluid Mechanics*, 48(1):365–391, 2016.

[26] H. P. Kavehpour. Coalescence of drops. *Annual Review of Fluid Mechanics*, 47:245–268, 2015.

[27] H. Lee, J. S. Lowengrub, and J. Goodman. Modeling pinchoff and reconnection in a hele-shaw cell. I. The models and their calibration. *Physics of Fluids*, 14(2):492–513, 2002.

[28] H. Lee, J. S. Lowengrub, and J. Goodman. Modeling pinchoff and reconnection in a hele-shaw cell. II. Analysis and simulation in the nonlinear regime. *Physics of Fluids*, 14(2):514–545, 2002.

[29] J. Liu, L. Dedè, J. A. Evans, M. J. Borden, and T. J. R. Hughes. Isogeometric analysis of the advective cahn-hilliard equation: Spinodal decomposition under shear flow. *Journal of Computational Physics*, 242:321–350, 2013.

[30] J. Lowengrub and L. Truskinovsky. Quasi–incompressible cahn–hilliard fluids and topological transitions. *Proceedings of the Royal Society of London A: Mathematical, Physical and Engineering Sciences*, 454(1978):2617–2654, 1998.

[31] J. A. Sethian. *Level Set Methods and Fast Marching Methods: Evolving Interfaces in Computational Geometry, Fluid Mechanics, Computer Vision, and Materials Science*. Cambridge Monographs on Applied and Computational Mathematics. Cambridge University Press, 1999.

[32] J. Shen and X. Yang. A phase-field model and its numerical approximation for two-phase incompressible flows with different densities and viscosities. *SIAM Journal on Scientific Computing*, 32(3):1159–1179, 2010.

[33] E. Shirani, N. Ashgriz, and J. Mostaghimi. Interface pressure calculation based on conservation of momentum for front capturing methods. *Journal of Computational Physics*, 203(1):154–175, 2005.

[34] R. H. Stogner and G. F. Carey. C^1 macroelements in adaptive finite element methods. *International Journal for Numerical Methods in Engineering*, 70(9):1076–1095, 2007.

[35] Y. Sun and C. Beckermann. Sharp interface tracking using the phase-field equation. *Journal of Computational Physics*, 220(2):626–653, January 2007.

[36] G. Tryggvason. Numerical simulations of the rayleigh-taylor instability. *Journal of Computational Physics*, 75(2):253–282, April 1988.

[37] S. Turek, A. Ouazzi, and J. Hron. On pressure separation algorithms (PSepA) for improving the accuracy of incompressible flow simulations. *International Journal for Numerical Methods in Fluids*, 59(4):387–403, 2009.

[38] J. D. van der Waals. The thermodynamic theory of capillarity under the hypothesis of a continuous variation of density. *Journal of Statistical Physics*, 20(2):200–244, 1979.